AGU PUBLICATIONS

Journal of Advances in Modeling Earth Systems

RESEARCH ARTICLE
10.1002/2015MS000447

PRYSM: An open-source framework for PRoxY System Modeling, with applications to oxygen-isotope systems

S. Dee[1], J. Emile-Geay[1], M. N. Evans[2], A. Allam[3], E. J. Steig[4], and D. M. Thompson[5]

[1]Department of Earth Sciences, University of Southern California, Los Angeles, California, USA, [2]Department of Geology and Earth System Science Interdisciplinary Center, University of Maryland, College Park, Maryland, USA, [3]Geophysical Institute, University of Alaska Fairbanks, Fairbanks, Alaska, USA, [4]Department of Earth and Space Sciences, Quaternary Research Center, University of Washington, Seattle, Washington, USA, [5]National Center for Atmospheric Research, Boulder, Colorado, USA

Key Points:
- A new modeling framework for paleoclimate proxies is proposed (PRYSM)
- PRYSM bridges the gap between GCMs and paleoclimate observations
- PRYSM may improve interpretation and uncertainty quantification of paleodata

Correspondence to:
S. Dee,
sdee@usc.edu

Citation:
Dee, S., J. Emile-Geay, M. N. Evans, A. Allam, E. J. Steig, and D. M. Thompson (2015), PRYSM: An open-source framework for PRoxY System Modeling, with applications to oxygen-isotope systems, *J. Adv. Model. Earth Syst.*, *7*, 1220–1247, doi:10.1002/2015MS000447.

Received 27 FEB 2015
Accepted 18 JUN 2015
Accepted article online 30 JUN 2015
Published online 18 AUG 2015

Abstract Paleoclimate observations constitute the only constraint on climate behavior prior to the instrumental era. However, such observations only provide indirect (proxy) constraints on physical variables. Proxy system models aim to improve the interpretation of such observations and better quantify their inherent uncertainties. However, existing models are currently scattered in the literature, making their integration difficult. Here, we present a comprehensive modeling framework for proxy systems, named **PRYSM**. For this initial iteration, we focus on water-isotope based climate proxies in ice cores, corals, tree ring cellulose, and speleothem calcite. We review modeling approaches for each proxy class, and pair them with an isotope-enabled climate simulation to illustrate the new scientific insights that may be gained from this framework. Applications include parameter sensitivity analysis, the quantification of archive-specific processes on the recorded climate signal, and the quantification of how chronological uncertainties affect signal detection, demonstrating the utility of **PRYSM** for a broad array of climate studies.

1. Introduction

Paleoclimate observations constitute the only constraint on climate system behavior prior to the onset of the instrumental record circa 1850. However, these records often prove difficult to interpret, as they may represent multivariate, nonlinear, biased, noisy and chronologically uncertain transformations of the input climate. Disentangling environmental influences on proxies is further confounded by nonstationarity and threshold dependencies within the climate system itself.

Traditional approaches to paleoclimatic reconstruction rely on empirical calibrations between measured variables and climate inputs; such inverse modeling of climate-proxy relationships represent these uncertainties in aggregate via calibration residuals. A complementary approach is to predict the measured value based on the environmental forcing and existing scientific understanding of the processes giving rise to the observation; models based on such a forward approach are known as proxy system models (PSM) [*Evans et al.*, 2013]. A PSM mathematically encodes mechanistic understanding of the physical, geochemical, and/or biological processes by which climatic information is imprinted and subsequently observed in proxy archives. Although PSMs may be multivariate and nonlinear, they are generally simplified representations of complete proxy systems; even so, they enable us to evaluate the extent to which assumptions often made by inverse modeling, such as stationarity and linearity, are valid.

PSMs have facilitated critical applications in paleoclimate science [*Evans et al.*, 2013], including, but not limited to:

1. Improved interpretation of climate signals embedded in proxy archives [*Anchukaitis et al.*, 2006; *Shanahan et al.*, 2007; *Sturm et al.*, 2010; *Lyons et al.*, 2011; *Tierney et al.*, 2011; *Brönnimann et al.*, 2012; *Baker et al.*, 2012; *Stoll et al.*, 2012; *Wackerbarth et al.*, 2012; *Steinman et al.*, 2013]
2. Isolating each transformation of the original climate signal, quantifying the contribution of each subsystem to observed model-data discrepancies [*Thompson et al.*, 2013a; *Dee*, 2013; *Dee et al.*, 2014a]
3. Enabling direct paleoclimate model-data comparison by bringing climate models into proxy space [e.g., *Thompson et al.*, 2011; *Russon et al.*, 2013; *Steig et al.*, 2013]

4. Paleoclimate state estimation (data assimilation) [*Steiger et al*., 2014]

5. Providing a data level for Bayesian hierarchical models [*Tolwinski-Ward et al*., 2013; *Tingley et al*., 2012]

6. Simulating the full range of possible error contributions by each subsystem (this study)

However, several challenges stand in the way of a broader use of PSMs. First, relatively few have been developed (for a review, see *Evans et al*. [2013]). Second, those that exist are currently scattered in the literature, making their integration by a single user difficult. Third, each model has been coded separately, in different programming languages, and according to disparate conventions. For broad-scale application of PSMs which span the range of proxy systems used in paleoclimatology, a standardized framework is required for their continued development and application.

In this paper we describe PRYSM (PRoxY System Modeling), a modeling framework for proxy systems. This framework is designed in Python, a well-supported open-source programming language already in broad use for analysis and visualization of climate data. Each PSM is designed around three submodels: sensor, archive, and observation [*Evans et al*., 2013]. This formalism allows all uncertainties to be treated consistently across different proxy systems, allowing the user to couple uncertainty along both axes (time and climate, roughly speaking). This initial iteration of PRYSM gathers PSMs centered around water isotope measurements (δ^{18}O, δD); however the framework is extremely general, and designed for extension to other measurement types.

The paper is organized as follows. Section 2 introduces the formalism of proxy system modeling, while the details of each system model are given in section 3. Section 4 highlights three of the many potential applications of this modeling framework, as well as an example of a multiproxy system model experiment combining all four available PSMs. The limitations and possible extensions of this work are discussed in section 5.

2. Proxy System Modeling

Paleoclimatic observations may be obtained from wood, coral aragonite, speleothems, ice cores, ocean and lake sediments, and many other sources (see NCDC, <http://www.ncdc.noaa.gov/paleo/datalist.html>). These observations are influenced by multiple environmental forcings, including temperature, precipitation, atmospheric circulation changes, and sea surface temperatures, for example [*Sturm et al*., 2010]. Table 1 describes some of their uses as records of climate system variability. To improve the interpretation of paleoclimate data, models that integrate climate and the processes by which proxy systems record climate are needed to distinguish between the target climate signal and auxiliary signals. In general, a transfer function (i.e., a PSM) is established to relate observed or modeled climate inputs (e.g., temperature, precipitation, isotopic compositions of precipitation, water vapor, or other relevant environmental variables) to the proxy measurement.

In addition, the use of paleoclimate data is affected by multiple uncertainties: not only is the climate signal recorded by the dependent variable (e.g., δ^{18}O) itself subject to error, but the independent variable (time) is

Table 1. Observation Types[a]

Archive	Location	Zone	Climate Variable
Trees	land	temperate	High-precision dating, high replication, drought records, *divergence problem for temp, potential for biological influence.*
Corals	ocean	tropics	Precise relative and absolute dating. Geochemically based, subannual to annual resolution, *potential for biological influence, sparse in time and space and not cross-dated.*
Ice Cores	land	high lat, high *z*	Myriad indicators. Precise relative dating. Interannual potential underused. *controls on tropical glaciers not constrained.*
Sediments	ocean + land	all	Myriad indicators. Resolution ranges from near-annual to multi-decadal at best, *often with large chronological uncertainties*. Mostly continuous.
Speleothems	land	all	precise absolute dating. *Climate interpretation equivocal.*

[a]Several different types of paleoclimate data are available (see NCDC, <http://www.ncdc.noaa.gov/paleo/datalist.html>). Each data type has its own benefits and shortcomings, and records changes on different time scales based on sampling resolution. Pros in normal font, cons in italics. Note: z= altitude.

indirectly obtained via chronostratigraphy or geochemical dating. The PSM framework can be leveraged to explicitly and jointly model these uncertainties on both axes (y: climate signal, x: time).

2.1. Modeling the Proxy Signal (*y* axis)

For each proxy class, *Evans et al*. [2013] distinguish between three main components of the proxy system response to climate forcing:

Sensor: physical, structural, and sometimes biological response of the medium to climate forcing.

Archive: mechanisms by which the proxy's sensor reaction is emplaced or deposited in a layered medium.

Observation: measurement made on the archive, accounting for effects related to sampling resolution in time and/or across replicates, choice of observation type, and age model.

PRYSM follows this framework and models these processes separately within dedicated modules. Using the oxygen isotopic composition (δ^{18}O) of tree-ring α-cellulose as an example, the *sensor* model encapsulates the processes by which environmental forcing (e.g., ambient or leaf temperature, humidity, and precipitation) is imprinted in the archive (e.g., cellulose component of wood). By choosing to observe the δ^{18}O of α-cellulose of latewood at a particular sampling resolution and level of replication across samples, we define the age model and choose the subset of environmental information encoded in the archive that is potentially accessible. In section 3, we illustrate these modules in more detail for the observation types currently represented in PRYSM.

A listing of paleoclimatic sensors, archives, observations, primary associated environmental forcings, and strengths and weaknesses for common sources of paleoclimatic information are in Table 1. In general, paleoclimatic sensors, archives and observations are segregated by geography, temporal resolution, chronological precision and accuracy, and environmental response, but a common feature is that many proxy systems represent many-to-one mapping of the environmental variable and temporal sampling to the observations we make in the archives. Because age uncertainty is of central importance for determining rates of change and identifying coherent spatial patterns, we next turn to the representation of age uncertainties within PSMs.

2.2. Modeling Time Uncertainties (*x* axis)

Paleoclimate observations often harbor significant age uncertainties, limiting our ability to accurately reconstruct high-resolution climate variability. While a number of studies have acknowledged and modeled the confounding effects of such age uncertainties [e.g., *Burgess and Wright*, 2003; *Bronk-Ramsey*, 2008, 2009; *Blaauw and Christen*, 2011; *Klauenberg et al*., 2011; *Parnell et al*., 2011b; *Scholz and Hoffmann*, 2011; *Anchukaitis and Tierney*, 2013], these errors are rarely propagated into climate reconstructions or model-data comparisons. PRYSM facilitates explicit propagation of random and systematic age uncertainties by incorporating recent age modeling tools into the PSM framework.

For most proxies in the geosciences, time is assigned to a depth horizon or ring/band feature via an age model. The latter may belong to two categories:

1. tie-point chronologies, such as most speleothem and sedimentary records, which use radiometric dates as tie points of the age-depth relationship;
2. layer-counted chronologies, such as corals, ice cores, tree-rings, varved sediments, and some speleothems, which are dated by counting layers formed by an annual or seasonal cycle, sometimes supplemented with independent age controls.

Uncertainties associated with these age models create significant challenges for time series analysis [e.g., *Comboul et al*., 2014], since these and other climate data analysis tools assume that the time axis is constrained at the level of the chronological resolution of the data. To allow for an assessment of the impacts of age uncertainties, we incorporate the errors associated with age assignments by tie points and/or layer-counting in the observation submodel.

2.2.1. Radiometrically Dated Proxies: Bchron

The modeling of tie-point chronologies has received much attention in the literature [*Bronk-Ramsey*, 1995; *Haslett and Parnell*, 2008; *Blaauw*, 2010; *Blaauw and Christen*, 2011; *Scholz and Hoffmann*, 2011; *Parnell et al*., 2011a; *Breitenbach et al*., 2012]. For such chronologies, many types of errors create uncertainty in estimates

of the timing of events, rates of change, stratigraphic correlations, and spectral analyses. These include analytical error, the error associated with radiocarbon calibration curves estimating calendar dates, and the interpolation of estimates to depth horizons for which no age information exists. A number of techniques have been developed for propagating these dating uncertainties into the interpretation of associated paleoclimate data. Radiocarbon age-depth modeling efforts have produced useful packages in R, including CLAM [*Blaauw*, 2010], BACON [*Blaauw and Christen*, 2011], Bpeat [*Blaauw and Christen*, 2005], OxCal [*Bronk-Ramsey*, 2008], and Bchron [*Haslett and Parnell*, 2008]. For speleothem records, published age modeling techniques include StalAge [*Scholz and Hoffmann*, 2011], mixed effect regression models [*Heegaard et al*., 2005], smoothing cubic splines [*Beck et al*., 2001; *Spötl et al*., 2006; *Hoffmann et al*., 2010], and finite positive growth rate models [e.g., *Drysdale et al*., 2005; *Genty et al*., 2006; *Hendy et al*., 2012]. Some of these methods are compared in *Scholz et al*. [2012].

While all of these methods are useful for producing realistic chronologies in the archives for which they were developed, we opted to include Bchron [*Haslett and Parnell*, 2008] in PRYSM v1.0, as it can be applied to any tie-point chronology, whether it involves a calibration (e.g., radiocarbon) or not (e.g., Uranium series). In addition, Bchron readily produces an *ensemble* of plausible chronologies, is easily modularized, open source, and requires few input parameters. Bchron uses a continuous Markov monotone stochastic process to simulate sample paths between constrained date horizons, and outputs an ensemble of age-depth relationships given partial dating information [*Haslett and Parnell*, 2008]. The model was originally developed to handle dating uncertainties in lake sediment cores, whose chronologies are based on radiocarbon (^{14}C) dates. Bchron is able to capture changes in accumulation rates, includes explicit handling of outliers, and simulates hiatuses in the data. These capabilities are crucial for records such as speleothems, whose age models often imply large variations in calcite precipitation (growth or extension) rate.

2.2.2. Layer-Counted Proxies: BAM

Comboul et al. [2014] recently developed a probabilistic model (BAM) for layer-counted proxies such as corals and tree-rings. The model accounts for both missed and doubly counted layers as a binomial or Poisson process, allowing for asymmetries in both rates over time. The study finds that time uncertainties at the annual scale significantly affect the spectral fidelity of high frequency (interannual) climate signals, and in some cases, decadal signals. For example, with a 5% error rate assumed for a coral time series, age errors between simulated chronologies can result in offsets of up to 10 years between 100-year long records. BAM produces an ensemble of plausible chronologies based on an *a priori* estimated error rates for under and overcounting. If additional information is provided, such an ensemble may be used to isolate an optimal chronology. In PRYSM, BAM is incorporated and applied to the coral, tree-ring cellulose, and ice core PSMs.

For either chronology type, the chronological uncertainty (x axis) is modeled as part of the observation submodel. The two axes are therefore naturally coupled within the PSM framework. Figure 1 shows example output for both of the age models employed in PRYSM. Both Bchron and BAM yield an ensemble of chronologies which can then be reassigned to the original data to explicitly simulate age errors.

2.3. A Generalized Uncertainty Model for PSMs

PRYSM enables the user to combine uncertainties in the proxy measurements and in chronological assignment explicitly. Errors are propagated from submodel to submodel, permitting quantification of uncertainty in a manner directly comparable to observations. At the same time, the modular structure of PRYSM permits submodel-level uncertainty analysis (Figure 2), allowing one to isolate error sources. Both these features are essential to the wise application of PSMs in paleoclimatology.

First, random error and systematic bias are present in the input data, whether historical or simulated using a general circulation model (GCM) (the "Environment" level in Figure 2). Uncertainties arise from limited data availability in time and space and from resolution and measurement biases. Second, structural uncertainty in the PSMs may be present as both random and systematic error. Structural uncertainties arise as a result of errors in the process representation, and can be assessed by implementing a suite of complementary submodels which differ slightly in their representation of the proxy's transformation of the climate signal, or by testing the PSM with a range of different GCM simulations. Parametric uncertainty exists at every tier of the PSM design. Each model contains a number of tunable parameters based on process-study or measurements spanning multiple sites/data networks; however, for some parameters, observational constraints are limited or not available. Further, parameter values may depend on regional or local conditions.

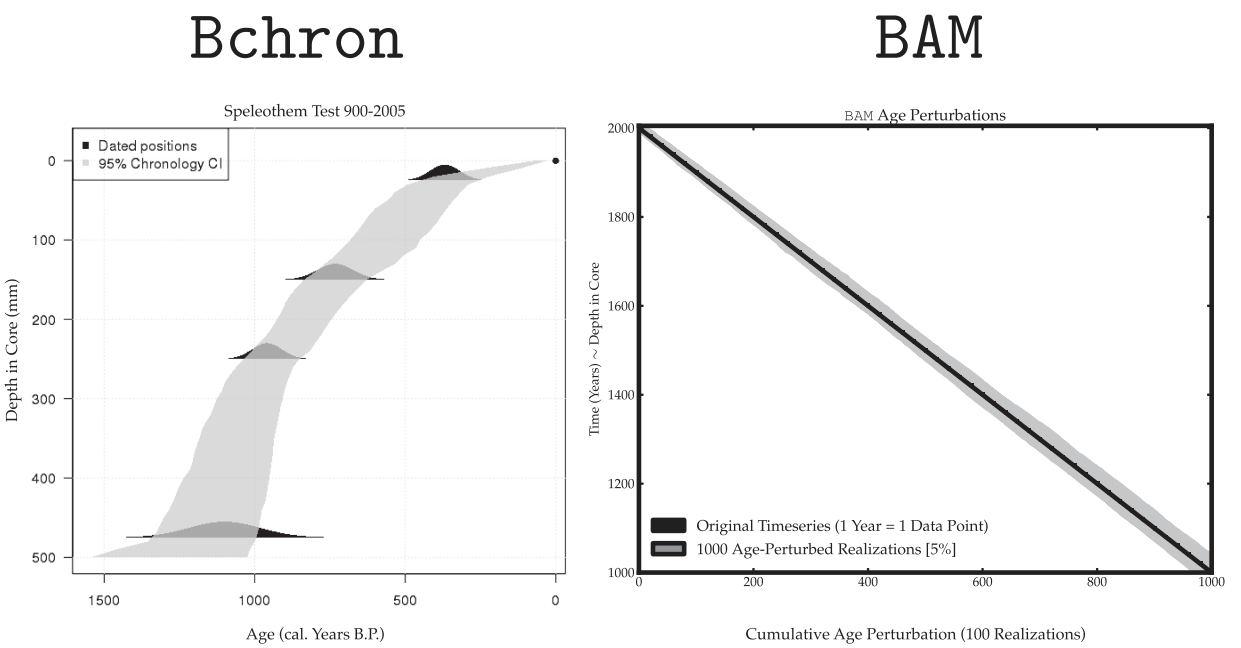

Figure 1. Age Models employed in PRYSM: Bchron, BAM. (left) Simulated age-depth horizons for a single cave record given five U/Th dates with errors. Bchron returns the 95% confidence intervals (in gray) for the age model based on input values for dates + uncertainties. This example assumes the top-most date is perfectly known (black dot at age 0), samples from a posterior distribution of the age ensemble, and allows for varying sedimentation rate. (right) Simulated chronologies perturbed using BAM plotted against the original time series (black). This example uses a symmetric dating error of 5%. Age uncertainties compound with time from the top-most date: the most recent dates are well constrained, while older dates (or dates from deeper in the sample) are subject to larger age errors. For the PSMs described in this work, BAM is used to model age uncertainties in layer-counted proxies (ice cores, corals, and tree ring cellulose), and Bchron is used for tie-point dating in speleothem calcite.

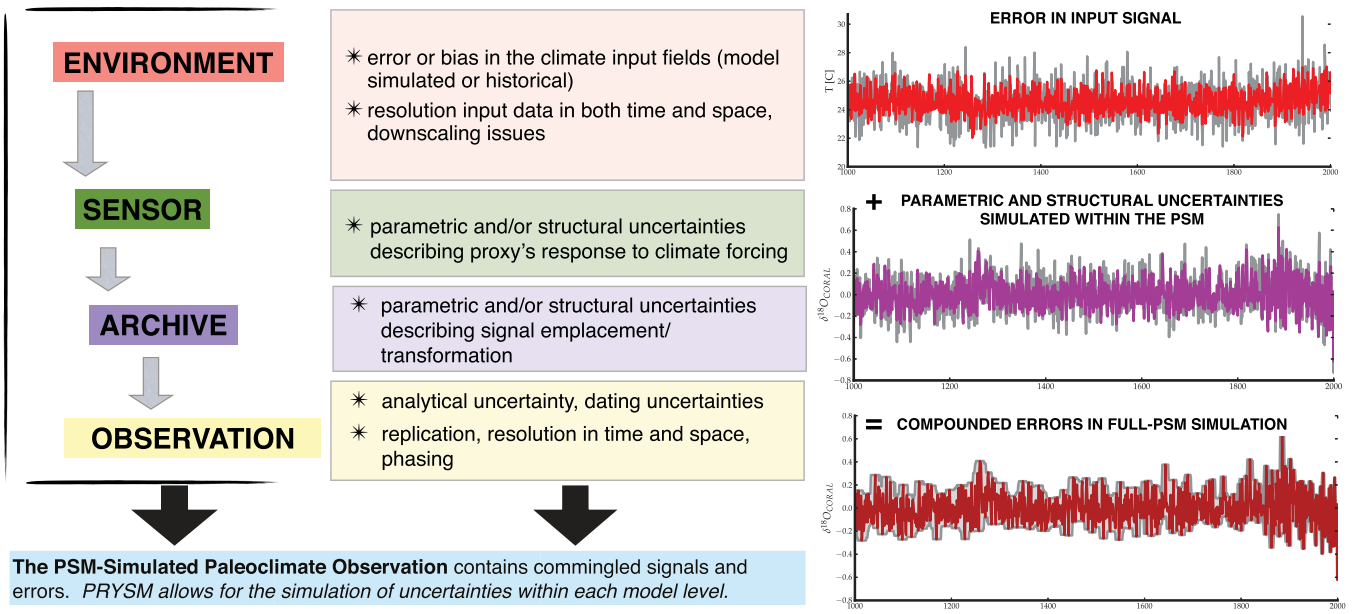

Figure 2. A Generalized Uncertainty Model for PSMs. PRYSM lays out a compartmentalized framework for identifying uncertainties. Uncertainty types may arise at each step of the submodel process (environment, sensor, archive, observation, simulated signal) (left) in a variety of common paleoclimatic archives, (right) as illustrated with a coral $\delta^{18}O$ example. Each submodel can be used to produce an ensemble of simulations that propagate structural, parameter, and input uncertainties. For example, parametric uncertainties at the sensor level may include the strength of a proxy response to local temperature, and at the archive level, due to processes such as diffusion or accumulation rates. "Phasing" uncertainty at the observation level refers to the fact that annually resolved input signals may miss seasonal impacts on proxy data (e.g., ENSO dynamics where an event lasts 6–18 months and may show highest expression in boreal winter). See text for details.

GCM-simulated input data additionally harbors parametric uncertainties (e.g., convective entrainment parameters in coarse-resolution GCMs). Finally, when simulated and actually observed paleoclimatic data are compared, errors resulting from resolution and downscaling (e.g., from GCM to proxy scale) may become apparent. Resolution in both time and space of the environmental inputs (observed or modeled) may differ substantially from the subgrid scale nature of point observations, as the observations respond to local or microclimate conditions, often within a growing or accumulation season.

As an illustrative example, we apply this generalized uncertainty model to map uncertainties for the $\delta^{18}O$ of coral aragonite (the full model is discussed in section 3.2). The environment submodel will harbor biases in the sea surface temperature (SST) and sea surface salinity (SSS) input variables. The sensor model contains structural uncertainties due to the choice to exclude the effects of photosynthesis, light, and nutrient availability on the corals; parametric uncertainties exist in the slope of the local coral-temperature response and the local relationship between SSS and the oxygen isotopic composition of the seawater. The archive model can consider structural uncertainty due to changes in accumulation or extension rate and preservation, and the observation model includes parametric uncertainties associated with the layer miscount rate (dating uncertainty), as well as analytical error.

The coding architecture of the modeling framework is designed to aid the user in disentangling error propagation. The relative effects of uncertainties in the time (x) axis on the captured climate signal axis (y) can be tracked. Finally, the submodel structure allows for the identification of those errors that dominate the final signal.

3. Modeling Water Isotope Proxies

We now describe models for four proxy systems, with reviews of the studies on which their formulations are based. We have incorporated the key functionalities of all published models, and defend our selections in each PSM description below.

3.1. Ice Core $\delta^{18}O$

Here we draw heavily from work simulating the $\delta^{18}O_{ice}$ at individual locations [*Vuille*, 2003; *Gkinis et al*., 2014], modeling diffusion in the firn [*Johnsen*, 1977; *Whillans and Grootes*, 1985; *Cuffey and Steig*, 1998; *Johnsen et al*., 2000; *Küttel et al*., 2012; *Gkinis et al*., 2014], and compaction down core [*Bader*, 1954; *Herron and Langway*, 1980; *Li and Zwally*, 2011; *Arthern et al*., 2010].

Figure 3 shows the schematic of the ice core PSM, which includes three submodels: psm.ice.sensor, psm.ice.archive, psm.ice.observation as described below. The model simulates how ice core values evolve an accumulation-weighted isotopic composition of precipitation to a final diffused time series with simulated age errors. Required inputs and outputs for the model are given in Table 2.

3.1.1. Sensor Model

The ice core sensor model calculates precipitation-weighted $\delta^{18}O_P$ (i.e., isotope ratio is weighted by the amount of precipitation that accumulates) and corrects for temperature and altitude bias between model and site ($-0.5‰/^{\circ}C$ [*Yurtsever*, 1975], $-0.3‰/100\,m$ [*Vogel et al*., 1975]). Precipitation weighting provides the best representation of strong seasonal changes (this is particularly important for tropical ice cores).

The ice core sensor model can be summarized as:

$$\delta^{18}O_{\text{ice}} = \frac{\sum(p \cdot \delta^{18}O_P)}{\sum p} + ac(\Delta z) \tag{1}$$

where p is precipitation amount, ac is an altitude correction (accounting for the potential for poorly resolved topography in climate models). Biases in precipitation may arise as a side effect of discrepancies in altitude or temperature as well, adding a level of uncertainty to the sensor model's simulation; we may attempt to address this additional bias in the next version of PRYSM.

3.1.2. Archive Model

Compaction and diffusion are considered as part of the ice core archive model.

3.1.2.1. Compaction and Density Profile

For this study, we employ the widely used steady state densification model of *Herron and Langway* [1980], using the mean annual temperature and mean annual snow accumulation rate as input variables.

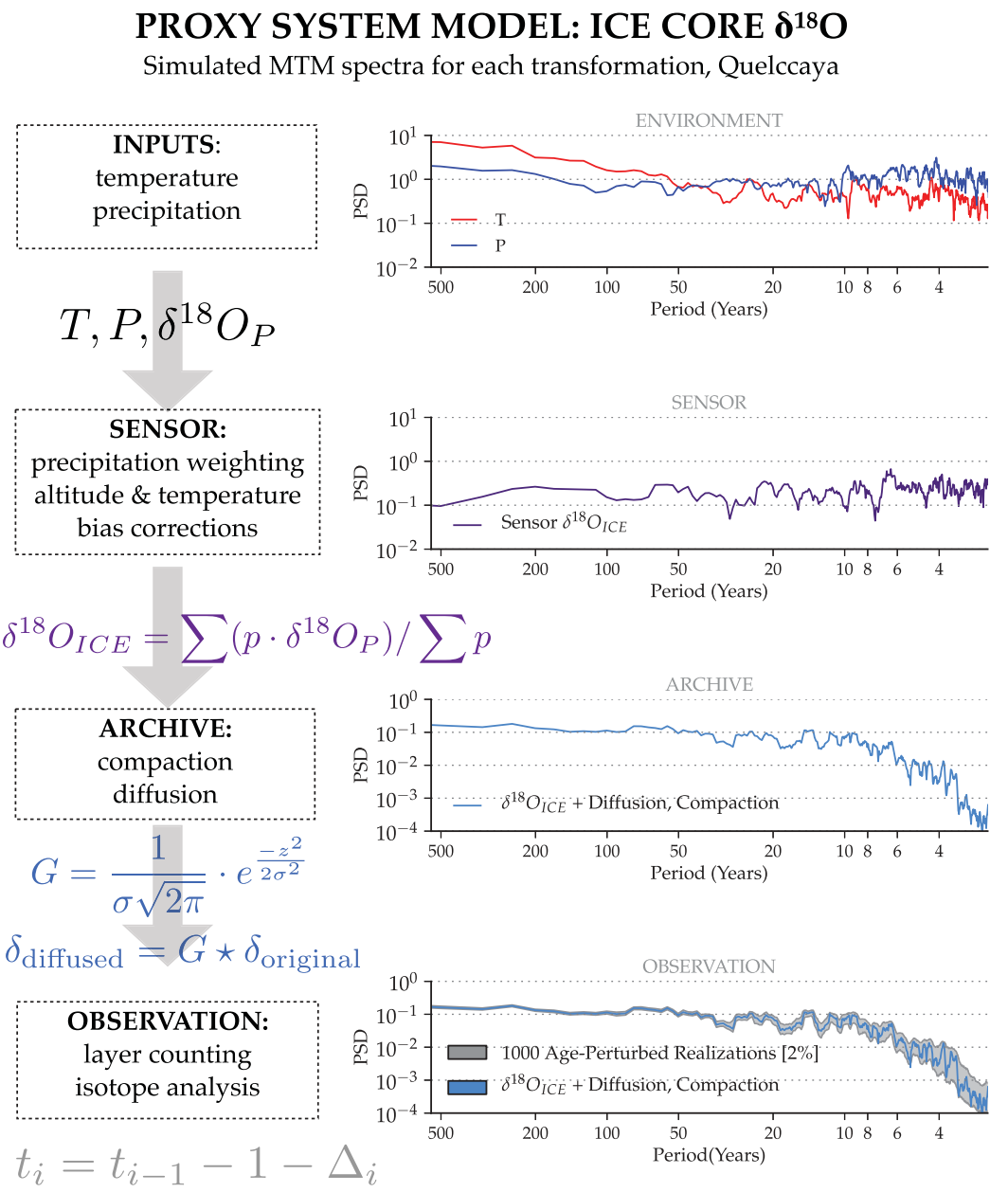

Figure 3. Proxy System Model: Ice Core $\delta^{18}O$. The ice core model takes the weighted $\delta^{18}O$ of local precipitation, applies an altitude correction, and allows for diffusion in the firn over depth. Dating uncertainties are modeled using BAM [*Comboul et al.*, 2014], specified as a 2% symmetric error.

Compaction is a function of the initial density (ρ) profile. The density versus depth profile is allowed to remain fixed in time. Although temperature and accumulation vary, the response time of the firn is very long (centuries to millennia, e.g., *Goujon et al.* [2003]), and can be neglected for typical applications such as

Table 2. Inputs and Outputs for Ice Core $\delta^{18}O_{ice}$ PSM in PRYSM v1.0[a]

Proxy Class	Inputs: Sensor	Inputs: Archive, Observation	PSM Output
Ice Core	Lat/Lon, p, T, $\delta^{18}O_P$, z	b, dz,T, θ, σ_a	D, σ, $\delta^{18}O_{ice}$ + BAM age model realizations

[a]Parameters: Lat/Lon: latitude and longitude coordinates, °; P: precipitation, mm/d; T: temperature, K; $\delta^{18}O_P$: isotope ratio of precipitation, ‰, z: elevation, meters (m) above sea level; dz: depth in core, annual layer depth, meters (m); b: accumulation rate, m.w.eq.a^{-1}; θ: age model uncertainty estimate, %; σ_a: analytical uncertainty, ‰, D: diffusivity (cm^2/s), σ: diffusion length, (cm).

reconstructions of the last few centuries. For very long time scales, or for large, rapid climate changes such as Dansgaard-Oeschger events, a time-dependent dynamic densification model [e.g., *Goujon et al*. [2003]; *Capron et al*., 2013] may be necessary but is not included here.

3.1.2.2. Depth Versus Age

The archive model next establishes a depth-age profile. Given a time series of isotope ratios, $\delta(t)$, each depth horizon (z) corresponds to time t. Annual precipitation accumulation rates are used to calculate the depth-age profile. The amount of diffusion that occurs depends on how long a section of the isotope profile remains at a given density; as the accumulation rate changes, the amount of time spent at a given depth (and density) varies, and adds additional low frequency variability to the signal. Note that it is convenient to have both z and t be positive downward (i.e., older snow at greater depth has greater t), such that t is the age of the snow, relative to the end point of the climate-modeled-time series. The time series of original δ values is converted from even spacing in time to even spacing in depth, using the relationship between $\delta(z)$, $\rho(z)$, and $t(z)$.

3.1.2.3. Diffusion

The amount of diffusion that occurs downcore is a function of the permeability of the firn, which determines how freely water vapor can move up and down the firn, and of temperature. Permeability is not well constrained by observations; however, much data on firn density have been collected, and firn density can be used as a reasonable proxy for permeability [*Whillans and Grootes*, 1985]. *Johnsen et al*. [2000] improved upon this by including a term for the tortuosity. In the model, firn density determines the diffusivity at each depth horizon. To establish the amount of diffusion that occurs at each layer in the firn, first a "diffusion length" is calculated. The diffusion length is the characteristic distance over which water molecules have moved up and down the firn, to produce the smoothed isotope profile. *Johnsen* [1977] and *Johnsen et al*. [2000] provide an elegant solution, showing that given the diffusion length σ, the isotope profile below the firn layer (i.e., once all diffusion except the slow diffusion in the ice has stopped) is simply the convolution:

$$\delta_{\text{diffused}} = G \star \delta_{\text{original}} \tag{2}$$

where $\star$ denotes convolution and G is a Gaussian kernel of standard deviation σ:

$$G = \frac{1}{\sigma\sqrt{2\pi}} e^{\frac{-z^2}{2\sigma^2}} \tag{3}$$

Note that the final post-diffusion isotope profile at a depth below the firn layer requires only one calculation, yielding the complete diffused profile. *Johnsen* [1977] showed that σ at the bottom of the firn layer is typically about 7 cm, and that locations with greater snow accumulation (which would tend to reduce the amount of diffusion that occurs) tend to be warmer locations (greater temperatures increase the diffusivity). Despite these potential simplifications, in this model, we require a complete isotope profile from the surface to the bottom of the firn. We make the calculation step-wise, using a new diffusion length at each time step [*Küttel et al*., 2012]. As discussed in *Cuffey and Steig* [1998], the diffusion length varies as $\sqrt{\bar{D}t}$, where $\bar{D}$ is the depth-integrated diffusivity and changes from zero at the surface to a constant value at the bottom of the firn. Note that we ignore the slow diffusion in solid ice, below the firn layer [*Johnsen et al*., 2000; *Cuffey and Steig*, 1998]. For each point in the discrete depth series of δ^{18}O, the entire depth-series $\delta_{\text{original}}(z)$ is convolved with the Gaussian filter (equation 3) using the single value of σ_i calculated for the depth $\rho(z)$. That data point is stored and the calculation is repeated for each point in the $\delta_{\text{original}}(z)$ data series to produce a final time series, $\delta^{\text{final}}_{\text{diffused}}(t)$.

3.1.2.4. Diffusion Length

The diffusion length is modeled similarly to *Cuffey and Steig* [1998] and *Johnsen et al*. [2000], following in particular the conventions of *Gkinis et al*. [2014]. Diffusivity, D, at depth z is calculated as a function of temperature and density, $\rho(z)$, and then integrated with respect to density. The integral over the density-dependent diffusivity, from the surface down to density ρ is:

$$\sigma^2(\rho) = \frac{1}{\rho^2} \int_{\rho_0}^{\rho} 2\rho^2 \left(\frac{d\rho}{dt}\right)^{-1} D(\rho) d\rho \tag{4}$$

where $\frac{d\rho}{dt}$ is the densification rate. This can also be thought of as the density profile in depth multiplied by the layer thickness: i.e., $\frac{d\rho}{dt}\frac{dt}{dz}\lambda = \frac{d\rho}{dz}\lambda$ where $\lambda = \frac{dz}{dt}$ is the annual layer thickness. This can alternatively be written:

$$\sigma^2(\rho) = \frac{1}{\rho^2}\int_{\rho_0}^{\rho} D2\rho^2\left(\frac{d\rho}{dz}\lambda\right)^{-1} d\rho \tag{5}$$

To make the calculation above, we require diffusivity as a function of density of the snow [*Johnsen et al*., 2000]:

$$D(\rho) = \frac{me_sD_{ai}}{RT\alpha_i\tau}\left(\frac{1}{\rho} - \frac{1}{\rho_{ice}}\right) \tag{6}$$

where m is the molar weight (kg), ρ is the density in kg/m^3 to yield diffusivity in m/s, ρ_{ice} is 920 kg/m^3, α_i is the ice-vapor fractionation for the water isotopologue $H_2^{18}O$, and D_{ai} is the diffusivity of the water isotopologue $H_2^{18}O$ ($D_a/1.0285$). D_a is the diffusivity of water vapor in air [*Hall and Pruppacher*, 1976]:

$$D_a = 2.1\cdot 10^{-5}\left(\frac{T}{T_0}\right)^{1.94}\left(\frac{P_0}{P}\right) \tag{7}$$

where P is the ambient pressure (Atm), $P_0 = 1$ Atm, T is ambient temperature (K) and $T_0 = 273.15$ K, R is the gas constant = 8.314478. In equation 6, τ is the tortuosity, and e_s is the saturation vapor pressure over ice:

$$e_s = \exp\left(9.5504 - \frac{5723.265}{T} + 3.530\cdot\ln(T) - 0.0073T\right) \tag{8}$$

Finally, for the tortuosity (τ), we use *Johnsen et al*. [2000]:

$$\frac{1}{\tau} = 1 - \dot{b}\left(\frac{\rho}{\rho_{ice}}\right)^2 \tag{9}$$

for $\rho \leq \frac{\rho_{ice}}{\sqrt{\dot{b}}}$, where $\dot{b}$ is the accumulation rate in meters of water equivalent per year (m.w.eq.a^{-1}). Following previous work, diffusion ceases at ρ=0.82, corresponding to the firn-ice transition [*Johnsen et al*., 2000]. We note that while diffusion does occur below this depth, the process is very slow in solid ice and can be considered negligible for most applications (e.g., climate proxy simulations occurring over a few thousand years) at most ice core locations [*Johnsen et al*., 2000; *Cuffey and Steig*, 1998]. Diffusion below the firn layer could be accounted for in future versions of PRYSM. The output of the ice core archive model is shown in Figure 4: for a simulated site (using parameters for Vostok, central East Antarctica, as an example), the model returns the age-depth relationship, diffusivity, diffusion lengths versus depth, and firn diffusion length over annual layer thickness.

3.1.3. Observation Model

The handling of age uncertainties (the observation model) in the ice core PSM is discussed in section 2.2.2, and uses BAM. We adopt a default value of 2% dating uncertainties in ice cores based on values reported in the literature [e.g., *Alley et al*., 1997; *Seimon*, 2003]. This value should be informed by measurement data on a site-by-site basis and warrants more detailed studies [e.g., *Steig et al*., 2005]. A short routine accounts for analytical uncertainty on laboratory measurements, adding a zero mean Gaussian process $\xi_a \sim \mathcal{N}(0, \sigma_a)$ to the modeled time series with a default value of $\sigma_a = 0.1‰$.

3.2. δ^{18}O of Coral Aragonite

δ^{18}O in living and fossil corals can help to reconstruct atmospheric and oceanic changes due to their sensitivity to the El Niño Southern Oscillation (ENSO), changes in sea surface temperatures (T), and salinity (S) [*Gagan et al*., 2000; *Corrège*, 2006; *Lough*, 2010]. Experimental and empirical studies of the inorganic and coral-mediated precipitation of aragonite from seawater have shown that variations in the δ^{18}O of coral aragonite are dependent on calcification temperature [*O'Neil et al*., 1969; *Grossman and Ku*, 1986; *Weber and Woodhead*, 1972] and the δ^{18}O of seawater from which the coral precipitated its aragonite; the latter, in turn, is closely associated with net freshwater flux from the surface ocean arising from net evaporation,

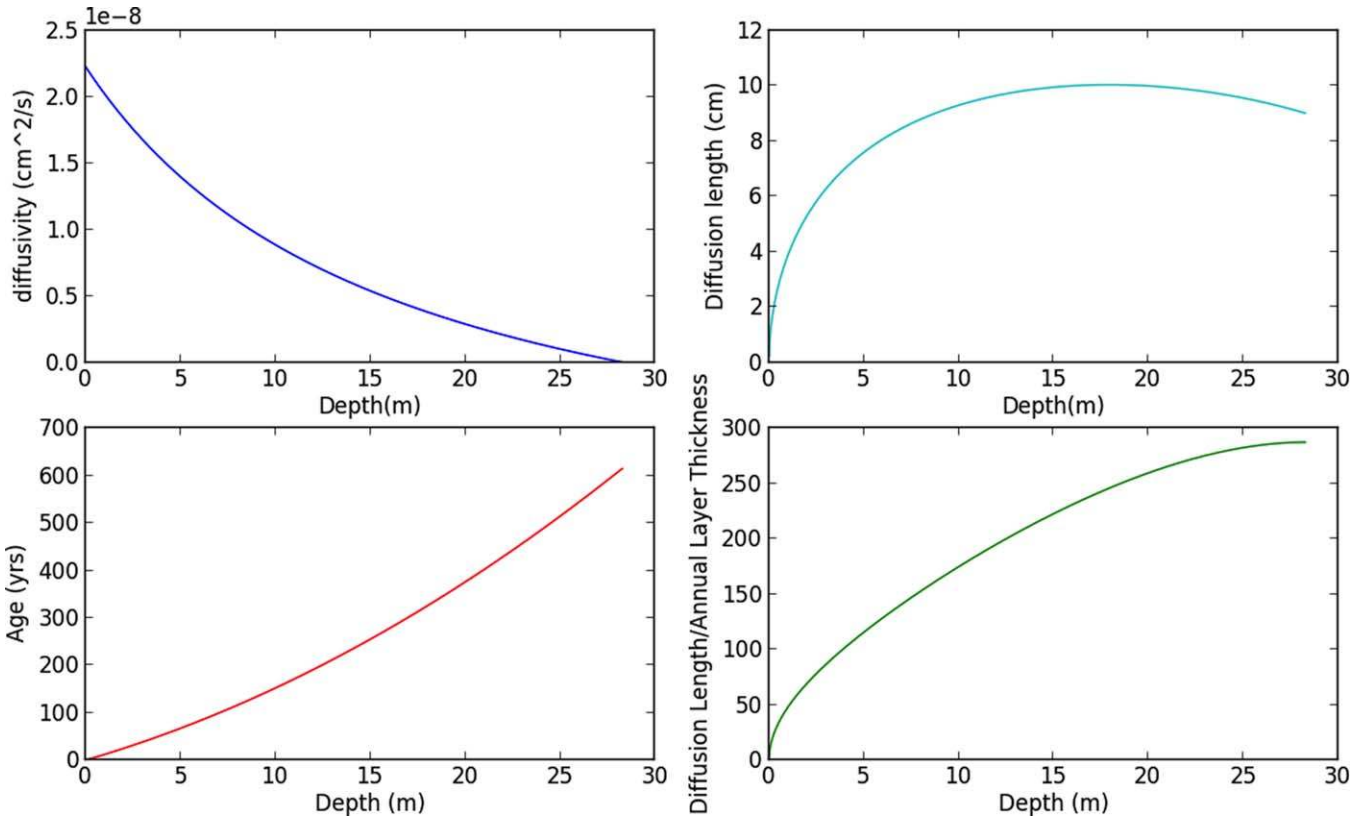

Figure 4. Proxy System Model: Ice Core $\delta^{18}O$ *(Archive)*. Within the Ice Core PSM, the ice sheet is the sensor, the ice is the archive, the δ^{18}O of ice is the observation. The ice core archive model accounts for compaction and diffusion in the firn. The compaction model is used to determine an age-depth relationship, and diffusivity is calculated for each point over depth. The figure shows an example output for Vostok, Antarctica: diffusivity with depth, diffusion length, and diffusion length over annual layer thickness to remove the effects of compaction. Diffusion length and diffusivity are intermediary variables within the PSM returned by the archive model.

condensation, runoff and water advection [*Craig and Gordon*, 1965; *Cole and Fairbanks*, 1990; *Wellington et al*., 1996; *Delcroix et al*., 2011], and is therefore linked to salinity.

Figure 5 shows the schematic of the coral PSM, which includes three submodels: psm.coral.sensor, psm.coral.archive, psm.coral.observation. Required inputs and outputs are given in Table 3.

3.2.1. Sensor Model

Thompson et al. [2011] developed a simple bivariate PSM for coral aragonite δ^{18}O anomaly as a linearized function of sea surface temperature and salinity anomalies; the latter, in turn, approximate variations in δ^{18}O of seawater associated with net freshwater flux from the surface and ocean mixed layer [e.g., *Fairbanks et al*., 1997]. This model has been employed to construct "pseudocorals" from the PSM coupled to observations of T and S and CGCM simulations [e.g., *Thompson et al*., 2011] and isotope-enabled GCMs [e.g., *Russon et al*., 2013; *Thompson et al*., 2013a] for comparison with actual coral δ^{18}O observations.

The anomaly model for δ^{18}O is written as:

$$\Delta\delta^{18}O_{\text{coral}} = \alpha\Delta T + \Delta\delta^{18}O_{\text{sw}} + \xi_m \tag{10}$$

where ΔT is the sea-surface temperature anomaly, α is an empirically determined coefficient specified by the relationship between oxygen isotopic equilibrium and formation temperature of carbonates [e.g., *Epstein et al*., 1953], $\delta^{18}O_{\text{sw}}$ is the anomalous oxygen isotopic composition of the ambient seawater, and $\xi_m \sim \mathcal{N}(0, \sigma_m)$ is an error term accounting for model misspecification. This term describes both random and systematic uncertainty (e.g., due to processes such as diagenesis) about $\delta^{18}O_{\text{coral}}$ that is not captured by the linear bivariate model, and its variance may be estimated via an analysis of regression residuals. *Thompson et al*. [2011] show how this forward model can be forced using both observed SST and $\delta^{18}O_{sw}$/S data and CGCM output. In practice, S observations and simulations are more readily available than $\delta^{18}O_{sw}$,

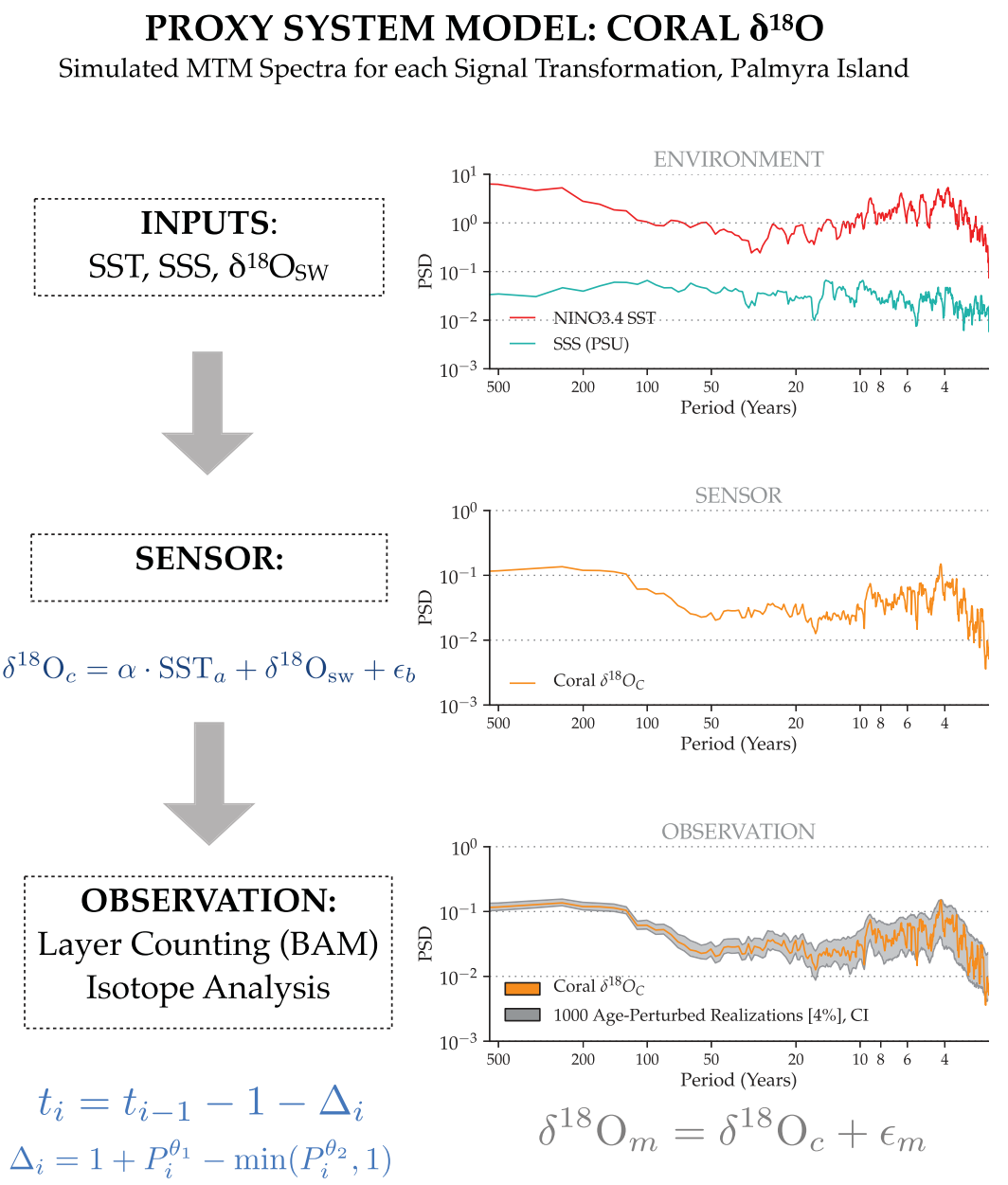

Figure 5. Proxy System Model: $\delta^{18}O$ of coral aragonite. The coral model accounts for sensitivity to SST and SSS (as per *Thompson et al.* [2011]), and explicitly models age uncertainties (5%) and analytical error (0.1‰).

for which no complete surface data set exists (but see *LeGrande and Schmidt* [2006], http://data.giss.nasa.gov/o18data/). The default value of α used in the model is $-0.22/^{\circ}C$ [*Evans et al.*, 2000; *Lough*, 2004], but the parameter can be externally specified. If $\delta^{18}O_{sw}$ is not available, it can be estimated from sea-surface

Table 3. Inputs and Outputs for Coral $\delta^{18}O_C$ PSM in PRYSM v1.0[a]

Proxy Class	Inputs: Sensor	Inputs: Archive, Observation	PSM Output
Coral	Lat/Lon, SST, (SSS **OR** $\delta^{18}O_{SW}$)	θ, σ_a	$\delta^{18}O_{aragonite}$ + BAM age model realizations

[a]Parameters: Lat/Lon: latitude and longitude coordinates, °; SST: sea surface temperature, K; SSS: sea surface salinity, PSU; $\delta^{18}O_{SW}$: isotope ratio of sea water, ‰; θ: age model uncertainty estimate (rate of miscount), %; σ_a: analytical uncertainty, ‰; $\delta^{18}O_{aragonite}$: isotope ratio of coral aragonite, ‰.

salinity anomalies as $\beta \cdot \Delta S$, where β is simply the regional $\delta^{18}O_{sw}$-SSS relationship, converted from VSMOW to VPDB [*Fairbanks et al*., 1997; *LeGrande and Schmidt*, 2006]:

$$\Delta\delta^{18}O_{coral} = \alpha\Delta T + \beta\Delta S + \xi_m \tag{11}$$

3.2.2. Archive Model

Currently, the archive model for corals is included only as a placeholder. For simplicity, the coral PSM Version 1.0 assumes that idealized sampling practices were followed [*DeLong et al*., 2013], and thus does not include the effects of sampling path, core angle offsets relative to growth rates, biological interference to annual banding, or diagenesis on the resulting measurements. One could envision adding submodules that mimic these processes.

3.2.3. Observation Model

Age uncertainties in the coral PSM are modeled using BAM (section 2.2.2), with user-defined, independent error rates (default for corals is θ=2.5% symmetric error) for missing and doubly counted bands. As before, analytical uncertainty is modeled by a zero mean Gaussian process $\xi_a \sim \mathcal{N}(0, \sigma_a)$, with a default value of σ_a=0.1‰. Generally, $\sigma_a \ll \sigma_m$ [*Evans et al*., 2013].

3.3. Speleothem δ^{18}O

The oxygen isotopic composition of stalagmite calcite is dependent on calcification temperature and the isotopic composition of drip water. The latter is a many-to-one combination of precipitation, evaporation, advection and mixing of meteoric, soil, ground and cave waters [*McDermott*, 2004; *Fairchild et al*., 2006a]. The most common interpretation for speleothem δ^{18}O is as a measure of rainfall, via the "amount effect" [*Dansgaard*, 1964; *Mathieu et al*., 2002; *Lee et al*., 2007]. However, several studies have underscored the importance of considering soil water and karst processes when interpreting cave dripwater [*Fairchild et al*., 2006b; *Baldini et al*., 2006; *Williams*, 2008; *Dreybrodt and Scholz*, 2011]. Our speleothem PSM is designed to help identify the primary influences on, and time scales resolved for, variations in speleothem δ^{18}O records, to facilitate accurate paleoclimatic interpretation. Many published studies have devised forward models of speleothem calcite for these purposes, including *Mühlinghaus et al*. [2009]; *Bradley et al*. [2010]; *Baker and Bradley* [2010]; *Baker et al*. [2012]; *Truebe et al*. [2010]; *Partin et al*. [2013]. The oxygen isotopic composition of speleothem calcite ($\delta^{18}O_c$) is generally approximated as a function of cave temperature, precipitation amount, simplified karst hydrology, and $\delta^{18}O_{precip}$ at the site. However, speleothem forward models are limited by varying initial and boundary conditions in the groundwater and precipitation schemes (such as the storage volume, outlet size, and transit times), which results in a large sensitivity of cave drip water to each of these initialized values [*Baker and Bradley*, 2010]. PRYSM implements the model of *Partin et al*. [2013], a lumped-parameter model which represents karst mixing with a single tunable parameter. This modeling choice constitutes a middle ground between the common assumption of $\delta^{18}O_c \propto -P$, and a more sophisticated approach such as that of *Baker and Bradley* [2010].

The full speleothem $\delta^{18}O_c$ PSM is summarized in Figure 6. Required inputs and outputs for the model are given in Table 4. This speleothem PSM can be used to explore hydroclimate variability as captured by a single record, or in observations across a network of caves expected to sense a common environmental forcing.

3.3.1. Sensor Model

The isotopic composition of the cave drip water ($\delta^{18}O_d$) is calculated using the weighted isotopic composition of precipitation that falls over the cave ($\delta^{18}O_w$):

$$\delta^{18}O_w = \sum p \cdot \delta^{18}O_p / \sum p \tag{12}$$

where p is the precipitation rate (mm/month) and $\delta^{18}O_p$ is the monthly average isotopic composition of the rainfall (‰). The user can alternatively specify the input as the isotopic composition of the upper soilwater layer ($\delta^{18}O_s$) if this field is available from an isotope-enabled GCM; using $\delta^{18}O_s$ carries the advantage of accounting for evaporative enrichment to the soilwater before it enters the karst.

This signal is further filtered by an aquifer recharge model [*Gelhar and Wilson*, 1974] simulating the effects of karst storage on cave dripwater. The physics of this aquifer model are entirely characterized by the mean transit time $\tau = \frac{\phi}{a}$ (months), where ϕ is the effective porosity of the aquifer (unitless) and a is an outflow

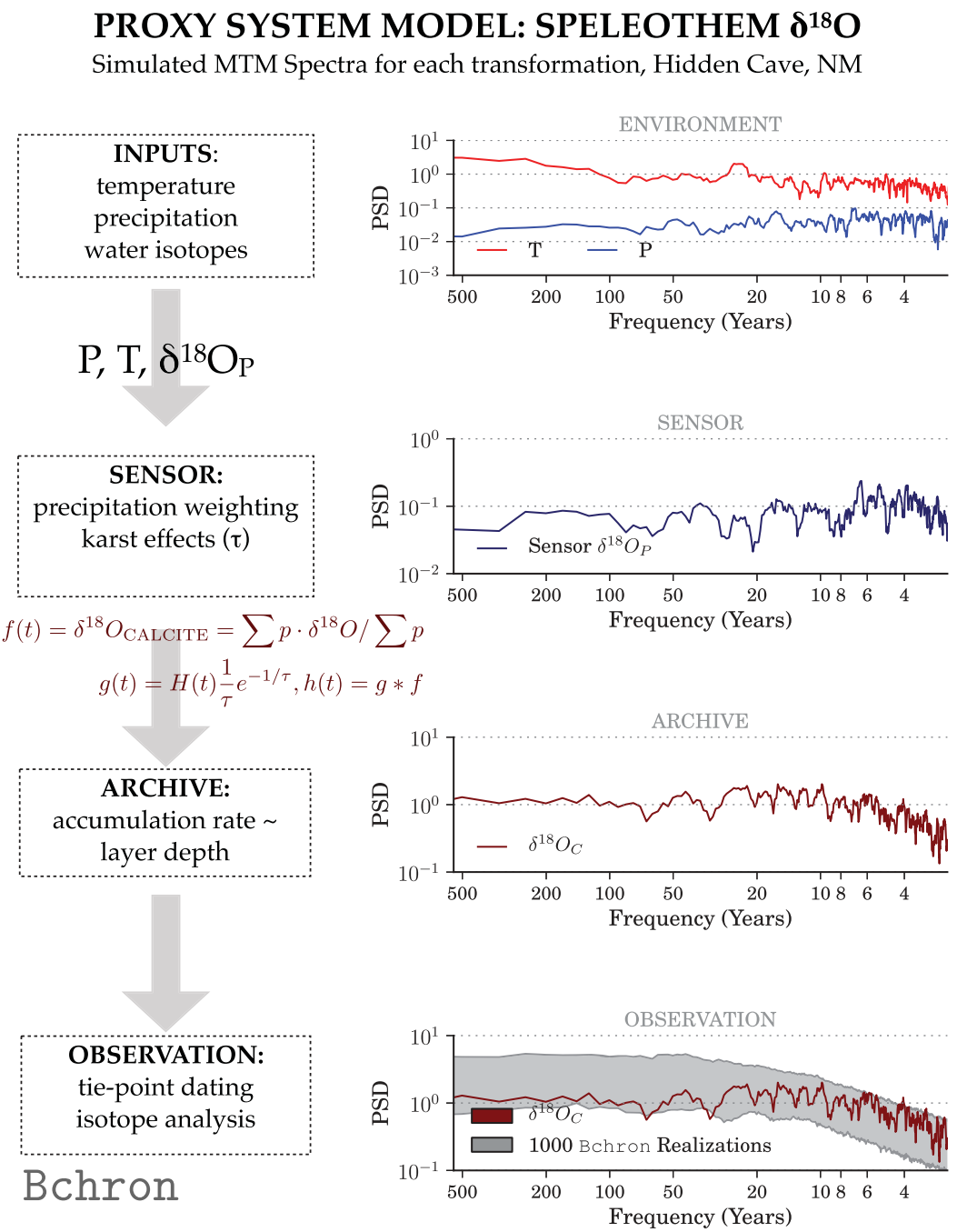

Figure 6. Proxy System Model: Speleothem $\delta^{18}O$ of Calcite. Cave dripwater is modeled using weighted $\delta^{18}O$ of local precipitation, convolved with a Gaussian filter to account for groundwater recharge and storage time. In this example, the groundwater transit time (τ) is taken as 1 year. Age model uncertainties are simulated using Bchron [*Haslett and Parnell*, 2008].

Table 4. Inputs and Outputs for Speleothem Calcite PSM in PRYSM v1.0[a]

Proxy Class	Inputs: Sensor	Inputs: Archive, Observation	PSM Output
Speleothem	Lat/Lon, T, $\delta^{18}O_P$, τ, ϕ	θ, σ_a	$\delta^{18}O_{\mathrm{calcite}}$ + Bchron age model ensemble

[a]Parameters: Lat/Lon: latitude and longitude coordinates (°); T: annual average temperature (K); $\delta^{18}O_P$: isotope ratio of precipitation (‰); τ: groundwater residence time (months); ϕ: porosity of aquifer (unitless); θ: age model uncertainty (for each tie-point date), %; σ_a: analytical uncertainty (‰); $\delta^{18}O_{calcite}$: isotope ratio of speleothem calcite (‰).

constant (months^{-1}). The aquifer recharge model may be represented by its impulse response (Green's function):

$$g(t)=\begin{cases}\frac{1}{\tau}e^{-t/\tau} & t>0\\ 0 & \text{otherwise}\end{cases} \tag{13}$$

Hence, for all positive times, the solution decays exponentially with *e*-folding time τ, which is also the mean residence time in the aquifer. The karst thus acts as a low-pass filter, introducing lags in the climate-proxy relationship (see section 4.1). The simulated drip water isotopic composition is thus the precipitation-weighted isotope ratio convolved with the karst's green function:

$$\delta^{18}\mathrm{O}_d = g(t) \star \delta^{18}\mathrm{O}_w \tag{14}$$

We note that in principle, τ can be estimated from observations of tracer dispersion in the karst, as done routinely in catchments [*McGuire and McDonnell*, 2006]. This simplicity is a distinct advantage over more complex models, whose many parameters are often difficult to constrain with scarce or regionally specific observations. This can lead to indeterminacy arising from parameter estimation as well as multivariate environmental forcing.

The $\delta^{18}\mathrm{O}_c$ of calcite recorded by the speleothem is finally subject to a temperature-dependent fractionation of the drip water ($\delta^{18}\mathrm{O}_d$) as the calcite precipitates [*Wackerbarth et al*., 2010, equation 11]:

$$\delta^{18}\mathrm{O}_c(\delta^{18}\mathrm{O}_d, T)=\frac{\delta^{18}\mathrm{O}_d+1000}{1.03086}\cdot \exp\left(2780/T^2-2.89/1000\right)-1000 \tag{15}$$

where T is the annual average temperature of the cave [K].

3.3.2. Archive Model

The speleothem archive model is currently included as a placeholder, and would serve to account for the effects of calcification rate on the retrieved $\delta^{18}O_c$ signal. We intend to include existing models for growth rate and calcite precipitation, following the efforts of *Kaufmann and Dreybrodt* [2004]; *Romanov et al*. [2008], and *Baker et al*. [2014], for example.

3.3.3. Observation Model

Age uncertainties in the speleothem model are modeled using Bchron [*Haslett and Parnell*, 2008], as described in section 2.2.1. Bchron can simulate piecewise continuous growth episodes (hiatuses), which are particularly common in stalagmites [*McDermott*, 2004]. As before, analytical uncertainty is modeled by a zero mean Gaussian process $\xi_a \sim \mathcal{N}(0, \sigma_a)$, with a default value of $\sigma_a = 0.1‰$.

3.4. Tree Ring Cellulose δ^{18}O

The oxygen isotopic composition of the α-cellulose component of wood depends on the isotopic composition of xylem water, evapotranspiration at the leaf or needle during photosynthesis, isotopic back diffusion at the leaf/needle between leaf/needle and xylem waters, partial reequilibration of photosynthate prior to cellulose synthesis, and the use of photosynthate reserves [*Roden and Ehleringer*, 1999; *Roden et al*., 2000; *Anderson et al*., 2002; *Roden et al*., 2002; *Barbour et al*., 2004]. In turn, the isotopic composition of xylem water has been shown to be unfractionated with respect to soil water [*Roden et al*., 2000, and references therein]; however, the isotopic composition of soil water may reflect rooting depth and variations in evaporation, precipitation, mixing and advection of precipitation, soil water and ground water.

Figure 7 shows the schematic of the isotopes in tree ring cellulose PSM, which includes two submodels: psm.cellulose.sensor, psm.cellulose.observation. Required inputs and outputs for the model are given in Table 5.

3.4.1. Sensor Model

The δ^{18}O of α-cellulose may be modeled as a fractionation relative to the isotopic composition of xylem water Δ [*Roden et al*., 2000; *Barbour et al*., 2004; *Evans*, 2007, and references therein]:

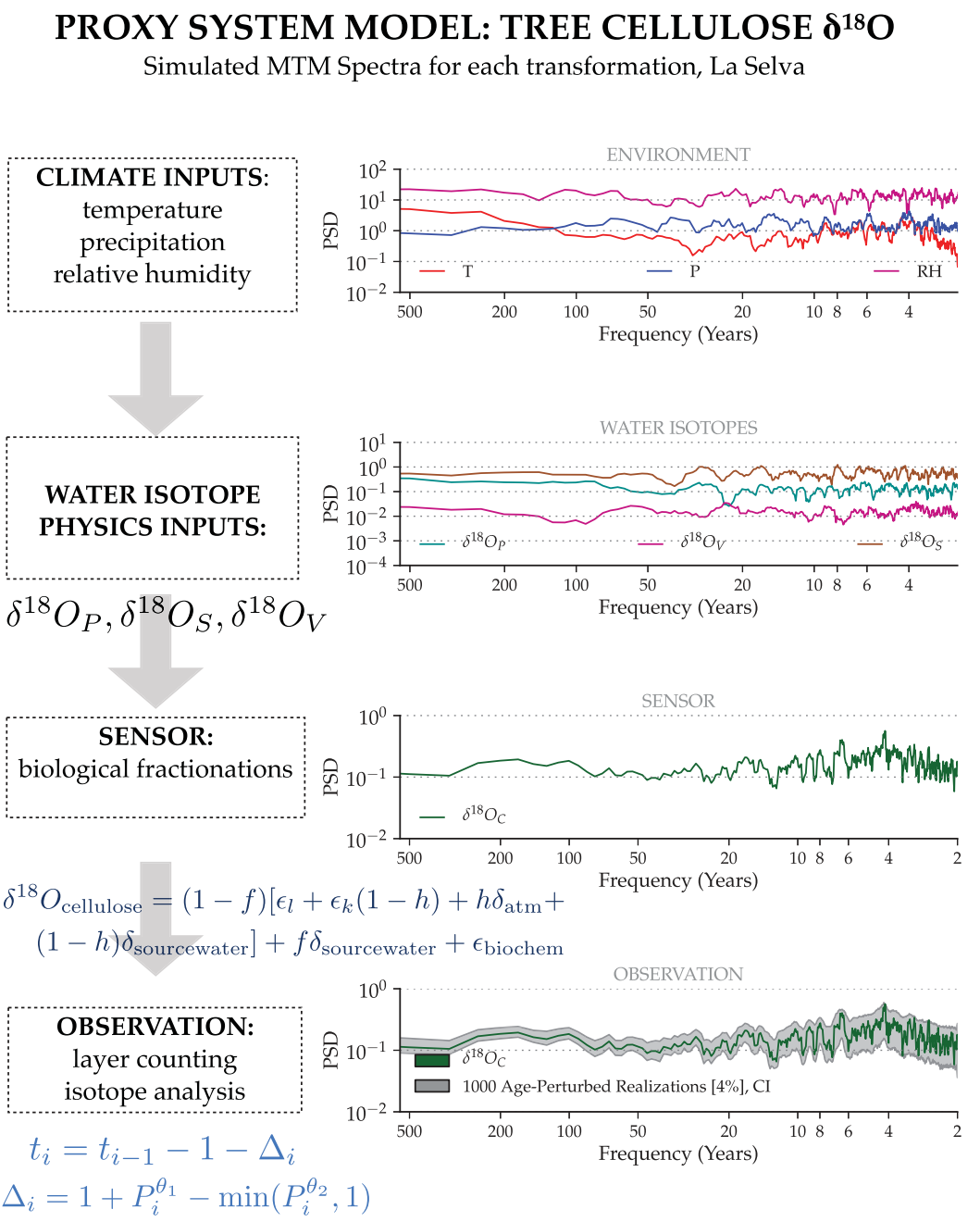

Figure 7. Proxy System Model: $\delta^{18}O$ of tree cellulose. Oxygen isotopes in tree cellulose are modeled after *Roden et al.* [2000]; *Barbour et al.* [2004]; *Evans et al.* [2006]; *Evans* [2007]. The PSM is modular, such that either the *Roden et al.* [2000] or *Evans* [2007]parameterization can be used interchangeably. Age uncertainties are modeled at a 1% symmetric error rate (i.e., 1 ring miscounted per 100 years), and analytical errors are taken as σ=0.1‰.

Table 5. Inputs and Outputs for Tree Ring Cellulose PSM in PRYSM v1.0[a]

Proxy Class	Inputs: Sensor	Inputs: Archive, Observation	PSM Output
Tree Ring Cellulose	Lat/Lon, P, T, RH, $\delta^{18}O_P$ ($\delta^{18}O_S$, $\delta^{18}O_V$ if available)	θ, σ_a	$\delta^{18}O_{cellulose}$ + BAM

[a]Parameters: Lat/Lon: latitude and longitude coordinates (°); P: precipitation (mm/d); T: temperature (K); RH: relative humidity (%); $\delta^{18}O_P$: isotope ratio of precipitation (‰); $\delta^{18}O_S$: isotope ratio of soil water (‰); $\delta^{18}O_V$: isotope ratio of ambient vapor (‰); θ: age model uncertainty estimate (rate of miscount), %; σ_a: analytical uncertainty (‰); $\delta^{18}O_{cellulose}$: isotope ratio of tree ring cellulose (‰).

$$\Delta^{18}O_{cellulose} = \Delta_{leaf}(1 - p_x p_{ex}) + \epsilon_c \tag{16}$$

with p_{ex} the fraction of oxygen atoms that have reequilibrated with xylem water prior to cellulose synthesis, p_x the proportion of xylem water in the cell forming the cellulose, and ϵ_c the equilibrium fractionation associated with biosynthesis of cellulose. The fractionation of leaf water relative to xylem water Δ_{leaf} [*Barbour et al*., 2004] is

$$\Delta_{leaf} = \frac{\Delta_e(1 - e^{-\mathcal{P}})}{\mathcal{P}} \tag{17}$$

with $\mathcal{P} = \frac{LE}{CD}$ the Peclet number, which is the ratio of convection, via transpiration at the leaf, of unenriched xylem water to evaporation sites, to the backward diffusion of $H_2^{18}O$ into the leaf. Convection is represented by *LE*, the product of the effective length *L* from evaporation surface and the evaporation rate *E*. Diffusion is represented by the diffusivity of $H_2^{18}O$ in water multiplied by the molar density of water *C* [*Barbour et al*., 2004]. Leaf level evaporative enrichment Δ_e is

$$\Delta_e = \epsilon^* + \epsilon_k + (\Delta_v - \epsilon_k)\frac{e_a}{e_i} \tag{18}$$

in which Δ_v is the oxygen isotopic composition of atmospheric water vapor relative to that of xylem water, and e_a and e_i are atmospheric and intercellular air water vapor pressures, respectively. The equilibrium and kinetic fractionation factors ϵ^* and ϵ_k are functions of temperature:

$$\epsilon^* = \exp\left(\frac{1137}{T^2} - \frac{0.4156}{T} - 0.0020667\right) - 1 \tag{19}$$

$$\epsilon_k = \frac{32r_s + 21r_b}{r_s + r_b} \tag{20}$$

with r_s and r_b the stomatal and boundary layer resistances to water flux from the leaf.

With specification of biophysical and environmental variables and parameters, Δ_{leaf} and Δ_c may be calculated, and with knowledge of $\delta^{18}O$ of source water, δ_{leaf} and δ_c may be predicted [*Barbour et al*., 2004]. With further parameterizations to define environmental parameters in terms of commonly measured direct meteorological observations and with additional simplifying parameterizations specific to tropical environments, *Evans* [2007] hypothesized that the $\delta^{18}O$ of α-cellulose from tropical trees should resolve the pattern of precipitation variation associated with ENSO activity. The PSM for water isotopes in tree-ring cellulose encoded in PRYSM v1.0 is similarly formulated to be driven with meteorological and isotopic data or simulations.

3.4.2. Archive Model

Similarly to the coral PSM, the PRYSM v1.0 wood PSM does not contain an archive model; an empty subroutine is included as a placeholder, but does not alter the output of the sensor submodel. However, an archive submodel for this PSM should include prior understanding of the growing season and/or seasonal hiatuses in growth over time [*McCarroll and Loader*, 2004], and effects of photosynthate storage from one growing season to the next [*Terwilliger*, 2003; *Roden et al*., 2002].

3.4.3. Observation Model

Age uncertainties in the tree ring cellulose PSM are modeled using BAM (Sec. 2.2.2.). The BAM default value for tree ring cellulose θ=2% symmetric error. As before, analytical uncertainty is modeled by a zero mean Gaussian process $\xi_a \sim \mathcal{N}(0, \sigma_a)$, with a default value of σ_a=0.3‰. For a single observation from a cross-dated tree ring, σ_a for α-cellulose is about 0.3‰. For annual averages of *n* independent monthly resolution estimates, $\sigma_a = 0.3/\sqrt{n}$. θ is bimodal: for cross-dated trees this value is approximately 1%, but for tropical trees, not cross-dated, not clearly annually banded, and with limited replication, the value of θ is much larger (4–5% or more). These values are user-specified.

4. Results: Simulating Step-Wise Signal Transformations

To demonstrate the utility of the PRYSM framework, we evaluate each transformation of the signal in a multi-PSM simulation using output from an isotope-enabled atmospheric general circulation model (AGCM) (SPEEDY-IER) [*Dee et al*., 2014b]. SPEEDY-IER is a new intermediate complexity, isotope-enabled AGCM designed for efficient ensemble simulations on paleoclimate timescales. The AGCM was used to simulate

the isotope hydrology and atmospheric response to SSTs derived from the "past1000" last millennium (850–1850) and "Last Millennium Extension" (1850–2005) PMIP3 integration of the CCSM4 model [*Landrum et al.*, 2013]. Each PSM was then driven with water isotope and climate fields from SPEEDY-IER to generate a synthetic proxy record at one of three different locations: Hidden Cave, New Mexico (speleothem), Quelccaya (tropical ice core), and La Selva, Costa Rica (cellulose), respectively, followed by a multiproxy application. Figures 4–7 show the decomposition of the climate signal for all of the PSMs included in PRYSM via spectral analysis. Each submodel filters the input climate signal uniquely, and the effect of each filter can be quantified in this framework. Here, we use three different PSMs to illustrate the impact of each submodel on the interpretation of proxy records.

4.1. Sensor Model Contribution

Here we explore the effect of karst transit times in the speleothem PSM sensor submodel driven by simulated isotopic variations in precipitation. Speleothem records from the southwestern United States have frequently been used to reconstruct Holocene hydroclimate variability in the United States [e.g., *Polyak and Asmerom*, 2001; *Polyak et al.*, 2001, 2004; *Ault et al.*, 2013a]. For several of these sites, speleothem time series (used as a proxy for precipitation amount) display scaling behavior that cannot be replicated by GCM simulations for precipitation of the last millennium [*Ault et al.*, 2013a].

When measuring isotope ratios in speleothem calcite, the assumption that isotope ratios in calcite reflect rainfall amount is complicated by processes such as thermal fractionation, evaporative enrichment in soils, vadose zone mixing, and other karst processes. Only by explicitly modeling such processes can one confidently attribute the origin of systematic differences between paleoclimatic observations and simulations. To demonstrate this, we modeled the $\delta^{18}O_{\text{calcite}}$ for a widely studied site: Hidden Cave, New Mexico. Figure 8 displays the simulated spectra of $\delta^{18}O_{\text{calcite}}$ using four values of the karst transit time τ, showing that it

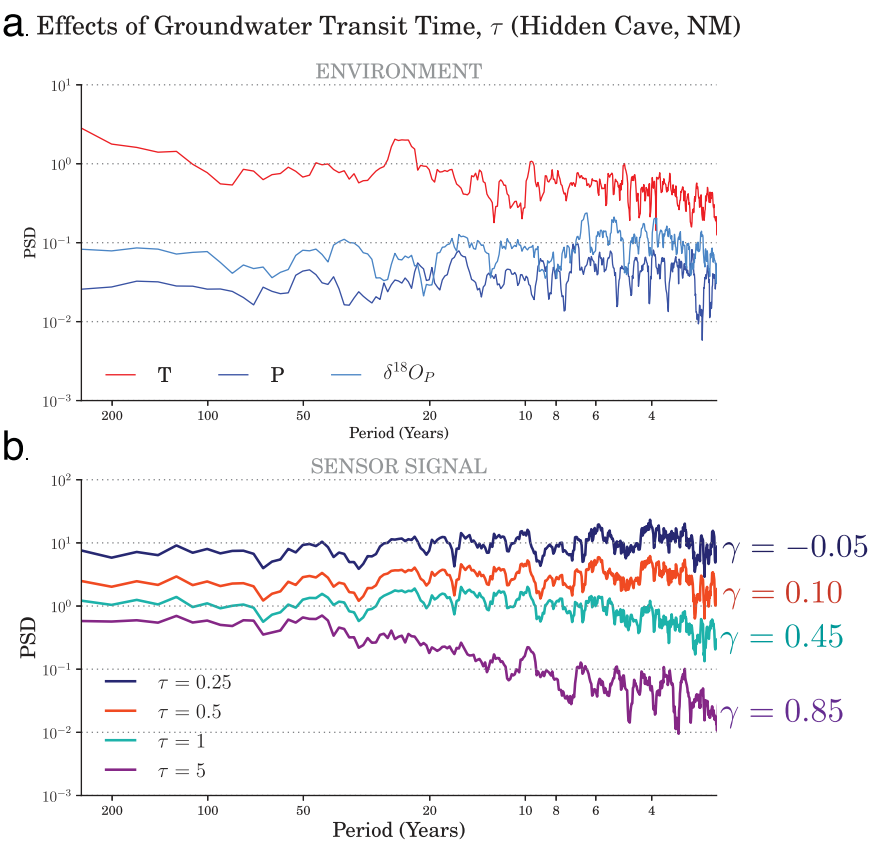

Figure 8. MTM-Spectra for simulated $\delta^{18}O$ of Speleothem Calcite at Hidden Cave, New Mexico. Changes to signal strength induced by varying karst transit times (τ, years) in the speleothem PSM sensor model. The figure indicates that scaling behavior can arise in the signal due to karst parameters alone; constraining a value for τ may thus prove crucial for interpreting high-resolution speleothem data. Values for the spectral slope (γ) are given for each value of τ.

exerts a first order control on the scaling properties of $\delta^{18}O_{calcite}$: short transit times (e.g., τ= 3 months) produce a $\delta^{18}O_{calcite}$ that is very similar to the input signal ($\delta^{18}O_P$, cobalt blue curve, Figure 8a.) while longer transit times (e.g., τ=5 years) result in a much steeper spectral slope, γ=0.85 (defined as $S(f) \propto f^{-\gamma}$) [see *Godsey et al*., 2010]. The values for the spectral slope (γ) observed given a range of plausible transit times (τ) are reported on Figure 8: for τ=0.25, 0.5, 1 and 5 years, γ=−0.05, 0.1, 0.45, and 0.85 respectively, indicating that γ is highly dependent on transit time.

For reference, *Ault et al*. [2013a] report a spectral slope of γ=0.82 using band thickness as a proxy for precipitation amount for the Hidden Cave data. These results are not directly comparable because of the different choice of precipitation indicator (band thickness versus $\delta^{18}O_{calcite}$), but the mismatch between the spectral slope of the input precipitation signal versus the final proxy signal is still apparent.

The chosen range in τ is representative of estimates for various karst systems. It is difficult to come up with an upper bound for this parameter, though expert elicitation suggests a number on the order of a few years (J. Kirchner and J. F. Clark, personal communication, 2014). While several studies have noted the importance of monitoring local meteorology at individual cave sites for growth rates [*Spötl et al*., 2005; *Baker et al*., 2014], little work has been done to constrain τ and its effects on the resulting $\delta^{18}O_{calcite}$ via site-based process studies. Recently, [*Moerman et al*., 2014] used paired measurements of rain and drip water oxygen isotopes at a site in Borneo and estimate $\tau \sim$ 3 months, but this is likely to be highly variable between cave systems and even between drips in the same cave [e.g., *Truebe et al*., 2010]. There is evidence for "old water" in groundwater [*McDonnell*, 1990; *Klaus and McDonnell*, 2013], suggesting that, in some environments at least, the limiting factor may be the transit time to the cave – not within the cave, where fractures may greatly accelerate the flow.

In this case, neglecting karst processes would lead one to erroneously blame GCMs for not producing the observed scaling behavior, while the fault may lie entirely in the karst. This highlights the necessity to ensure that (a) the model is structurally correct; (b) its parameters are experimentally constrained. Sensitivity experiments show that such scaling behavior is qualitatively similar with other models for karst mixing (e.g., advection-dispersion, leading to fractal scaling in solute concentrations [*Kirchner et al*., 2001]), so parametric uncertainty dominates structural uncertainty. Constraining a value for τ may thus prove crucial for interpreting high-resolution speleothem data.

The sensitivity of scaling exponents to the karst parameter motivates a more systematic characterization of transit times in karst systems in a range of climate regimes. More broadly, it illustrates how PRYSM may be used for identifying parameters that require further observational constraints. Alternatively, one can conceive of more complex karst and cave models [e.g., *Hartmann et al*., 2013], which will be included in future versions.

4.2. Archive Model Contribution

The PSM framework also allows an estimation for the time scales of climate variability that can be faithfully resolved by a proxy system. As illustrated in Figure 4 (Row 3), the contribution of the archive model can be isolated to address this question. We use a well-known tropical ice core as an example [Quelccaya, Peru: *Thompson et al*., 1985; *Thompson et al*., 2006, 2013b]. The total variance captured by the original climate $\delta^{18}O_P$ is damped by diffusion and compaction processes down core. Figures 4 and 9b show that diffusion and compaction disproportionately affect high-frequencies (see dashed versus solid line in Figure 9b), but leave low-frequencies intact. We here investigate how these processes affect the retrieval of climate information in simulated versus real-world observations.

PRYSM facilitates direct comparison of observations to simulations, intermodel comparison, as well as an investigation into the causes of model-data discrepancies. For Quelccaya in particular, the modeled and observed data tell two very different stories. While the archive submodel experiments suggest climate signal damping due to diffusion, the Quelccaya ice core record has been shown to capture near-annual variability reflecting changes in tropical sea surface temperatures [*Thompson et al*., 2013b]. Indeed, Figure 9a shows the correlation between SPEEDY-IER surface temperatures and simulated Quelccaya $\delta^{18}O_{ice}$: in agreement with *Thompson et al*. [2013b], the water isotope signal in the simulated ice core is strongly correlated to tropical pacific sea surface temperatures (R^2=0.46, QUEL v. NINO34).

It would be tempting to see the PSM validated at this point. However, Figure 9b shows the modeled time series for Quelccaya $\delta^{18}O_{ice}$ using water isotope output from both SPEEDY-IER and ECHAM5-wiso (a higher-order GCM) [*Werner et al*., 2011] alongside the measured values [*Thompson et al*., 2013b]. A

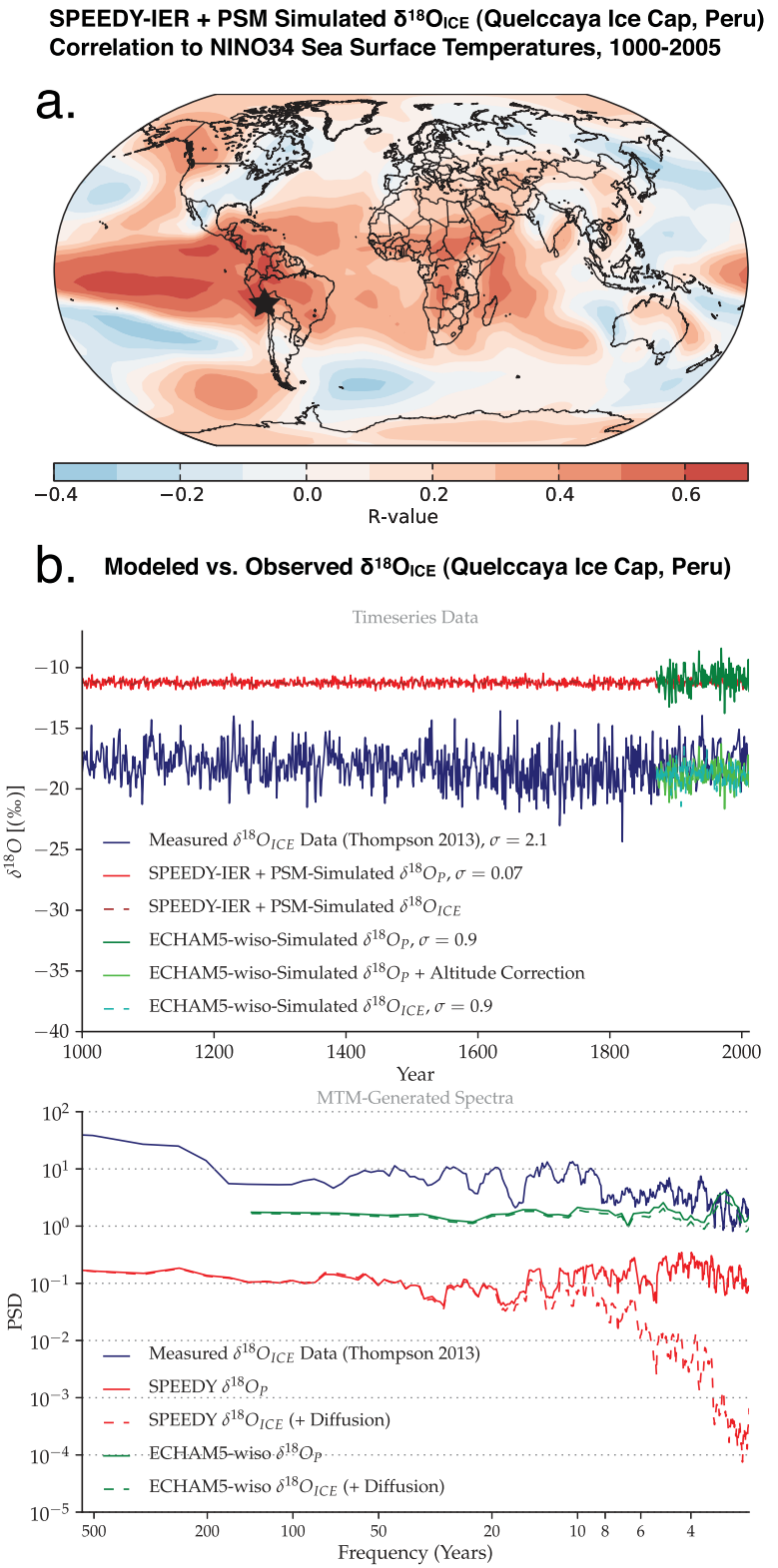

Figure 9. Model-Data Comparison: Ice Core PSM Archive Model, simulated and observed $\delta^{18}O_{ICE}$. (a) Correlation between simulated $\delta^{18}O_{ICE}$ at Quelccaya, Peru and modeled global SST. Maximum correlation between tropical pacific SSTs and $\delta^{18}O$ at Quelccaya in SPEEDY-IER: $R^2 = 0.46$. *Thompson et al.* [2013b] report $R^2 = 0.53$ for the (QUEL, NINO4) extended reconstruction from ERSST. (b) Modeled versus observed $\delta^{18}O$ time series and MTM-generated spectra for measured [*Thompson et al.*, 2013b] versus modeled (iso-GCM + ice core PSM). We compare the ice core PSM forced with data from both ECHAM5-wiso and SPEEDY-IER. PRYSM illustrates the value of explicit modeling of the physical processes for the identification of systematic error in the simulations.

comparison of low-order statistics reveals that the ice core PSM forced with SPEEDY-IER output differs significantly from observations. The mean isotope values in the SPEEDY-IER simulated data are offset from observations by $\sim+7‰$. Perhaps more striking is the difference in variance between the two records ($\sigma_{obs}=2.1‰$, $\sigma_{model}=0.07‰$). For ECHAM5-wiso, the comparison of the mean is much better once an altitude correction has been applied (via the ice core sensor model), but modeled variance is still less than half of the measured data: ($\sigma_{model}=0.9‰$) (see Figure 9b). Similar results were obtained by *Tindall et al.* [2009] (see Figure 4), modeling isotopes in precipitation using HadCM3 for a number of ice core sites including Quelccaya. The standard deviation of the HadCM3-simulated $\delta^{18}O_P$ is approximately 0.5‰, as compared to 1.5‰ observed. Care is needed to diagnose the causes of divergence between simulated and observed proxy data, but the divergence in itself yields valuable information for constraining each GCM. It sparks an investigation to identify the source of the discrepancy: is the problem a poor climate simulation, a poor isotope physics scheme, or a structural or parametric uncertainty in the PSM?

We first note that orography is poorly resolved in both SPEEDY-IER and ECHAM5, especially over the Andes. Will an altitude or temperature correction to the water isotope fields suffice? Figure 9b shows that in the case of ECHAM5-wiso, the answer is yes, but only for the mean. Indeed, even with an altitude correction for the water isotope physics, the variability observed in the water isotope fields is lower than observations: while ECHAM5-wiso simulates variability closer to measured values, the variability in SPEEDY-IER is off by an order of magnitude. One clue comes from comparing accumulation rates: in ECHAM5, accumulation is 3.09 m/yr on average, versus 1.27 m/yr for SPEEDY-IER. This difference has a large impact on the relative expression of diffusion in each modeled ice core, as show in Figure 9b. The loss of variance due to diffusion in the ECHAM5-wiso simulation is minimal compared to SPEEDY-IER. It is possible that further data/model discrepancies arise from PSM defects, but in this instance, the burden seems to fall largely on the GCM's shoulders.

Within the GCM+PSM framework, these and other questions can be tackled within a closed system of assumptions. The disagreement between the modeled and observed Quelccaya record illustrates the complications that may arise in data-model comparison across all proxy classes. Ultimately, one of the main goals of developing PRYSM is to enhance the ability of proxy data to constrain climate models. The mismatch at Quelccaya provides a robust benchmark for improving the GCM water isotope simulation over the tropics and at high altitudes. In this example, the data-model comparison highlights shortcomings in both the GCM and the PSM. The advantage is that each of those shortcomings can be identified and compartmentalized.

4.3. Observation Model Contribution

In this section, we explore the impacts of age uncertainties in climate reconstructions. As shown in the bottom panel of Figures 4–7, dating uncertainties may significantly alter the final signal's spectrum. To further explore the practical consequences of this transformation, we take the example of tree-ring cellulose at La Selva, Costa Rica. Isotope ratios in tree cellulose at this site have been shown to seasonally record variability in the El Niño-Southern Oscillation (ENSO) through a sensitivity to positive summer rainfall anomalies during ENSO warm phase events [*Evans and Schrag*, 2004; *Evans*, 2007]. The age model for water isotopes in tree-ring cellulose is generally established assigning each isotopic minima to July annually. For La Selva, age model errors are estimated as ±2 years [*Evans and Schrag*, 2004]. To see how dating uncertainties may alter the retrieved climate signal, we thus impose a symmetric miscounting rate of $\pm2\%$ and quantify how the relationship of $\delta^{18}O_{\text{cellulose}}$ to a common ENSO index (NINO3.4) is altered.

We do so by regressing the La Selva modeled $\delta^{18}O_{\text{cellulose}}$ and NINO3.4 SST for each realization of the age model. Figure 10 shows 1000 age realizations (generated by BAM) of the original signal given dating errors (assuming 4 rings are miscounted for every 100 years), and the regression between NINO3.4 SST and the $\delta^{18}O_{\text{cellulose}}$ for both the unperturbed signal and the perturbed realizations of the signal. Without age uncertainties, there is a significant correlation between tree ring $\delta^{18}O_{\text{cellulose}}$ and the NINO3.4 index ($R=-0.52, p \ll 0.001$). (We note, however, that there are assumptions in the simulations that might produce correlations much higher than typically observed). As shown by the grey lines, this correlation is reduced to almost zero for all of the age-perturbed realizations.

The disruption to the climate signal at one site is exacerbated in the network context. If we extend this experiment to a network of sites, the first principal component (PC1) of a simulated cellulose network representing a realistic spread of data from tropical trees can faithfully resolve ENSO with as few as eight sites, due to dominance of the "amount effect" in the model. However, the presence of age uncertainties can

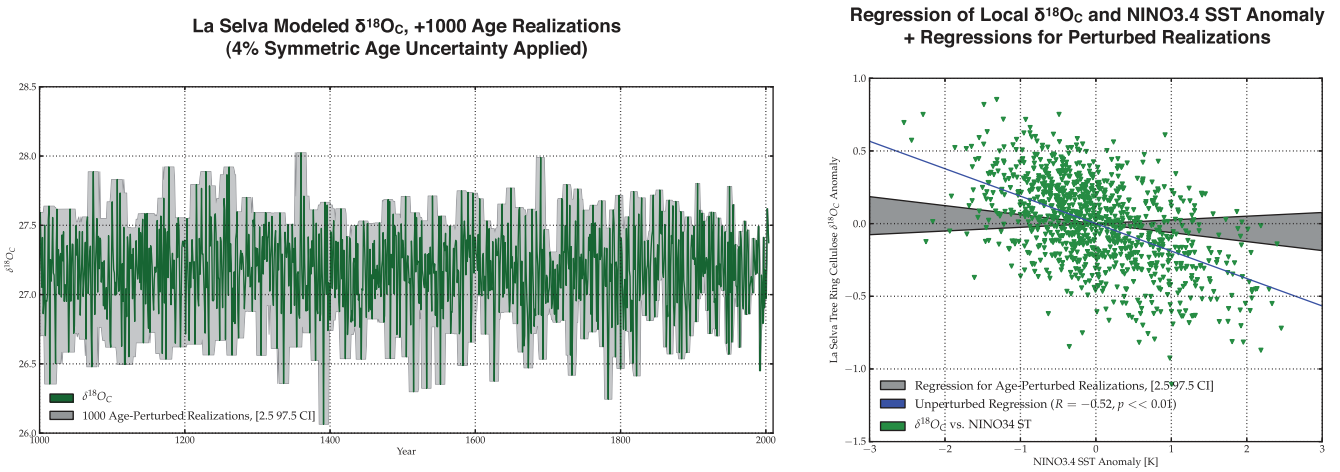

Figure 10. BAM-simulated tree cellulose chronologies given layer-counting errors. (left) The effects of age uncertainties for noncross dated cellulose records: plausible chronologies are plotted in gray around the "true" time series plotted in green. If calibrations are performed over the instrumental period with well-dated trees, it is tempting to assume the retrieved signal is robust. When age uncertainties are modeled explicitly, however, we can quantify the impacts of these errors. (right) Regression for $\delta^{18}O_C$ at La Selva and NINO3.4 SST for the unperturbed signal (blue line) and the regression calculated for 1000 realizations of the original signal given 4% symmetric age errors (gray). It is evident that the information contained in the original signal is lost with increasing age uncertainties.

significantly damp this signal, as shown in *Comboul et al.* [2014]. By explicitly modeling the range of plausible chronologies for a single record, this experiment illustrates how dating uncertainties in annually dated tree-ring cellulose can virtually annihilate the common climate signal in tropical trees, and reaffirms the importance of cross-dating in such studies [*Brienen et al.*, 2012; *Dee et al.*, 2014a].

4.4. A Multiproxy Application

A major benefit of PRYSM is the ability to simulate multiproxy networks. This is relevant to the statistical reconstruction of large-scale phenomena like ENSO [*Braganza et al.*, 2009; *Wilson et al.*, 2010; *Emile-Geay et al.*, 2013a, 2013b; *Ault et al.*, 2013b; *Tierney et al.*, 2015]. Here we investigate how four separate proxy types centered around the eastern tropical Pacific record and jointly filter a single climate signal (ENSO variability), and discuss implications for paleoclimate reconstructions.

Figure 11 shows the spatial correlation between surface temperature as well as $\delta^{18}O_P$ and NINO3.4 SSTs in a last-millennium simulation of SPEEDY-IER. Four proxy sites are shown on the map, along with the regression of the simulated $\delta^{18}O$ in each proxy on NINO3.4 SST anomalies. As demonstrated by Figure 11, interpretation and retrieval of the underlying climate signal is affected by both the proxy type and location.

The observed differences in the proxies' responses to a common forcing has implications for pseudoproxy experiments (PPEs) [*Smerdon et al.*, 2011]. PPEs are often used, by analogy, to evaluate climate field reconstruction methodology [e.g., *Smerdon et al.*, 2010], network sufficiency [e.g., *Wang et al.*, 2014], and skill [e.g., *Smerdon et al.*, 2011], subject to assumptions about observational uncertainty, observing network, and proxy system model (e.g., *Evans et al.*, 2014). The uncertainty in the pseudo observations used in PPEs may be described in terms of a "signal to noise ratio" (SNR), defined as:

$$SNR = \frac{|R|}{\sqrt{1-R^2}} \tag{21}$$

where R is the correlation of the local target reconstruction variable with the paleoclimate observation [*Mann and Rutherford*, 2002]. PSMs permit developing SNR estimates that are more representative of the nature of the different proxy systems, and thereby create PPEs that are more representative of the properties of actual CFRs. To illustrate this, we computed SNR for sensor models from four proxy systems (Figure 11) that are used to reconstruct measures of ENSO, here represented by the NINO3.4 SST anomaly index (160E–150W, 5N–5S). Extending this analysis, Table 6 gives the correlation and SNR for the sensor, archive and observation models (applied in succession) for each proxy system with the NINO3.4 index.

Table 6 indicates that based on the sensor models alone, each proxy produces a very different SNR (1.13, 0.23, 0.9, and 0.17 for tree ring cellulose, ice cores, corals, and speleothems, respectively). A higher SNR indicates that

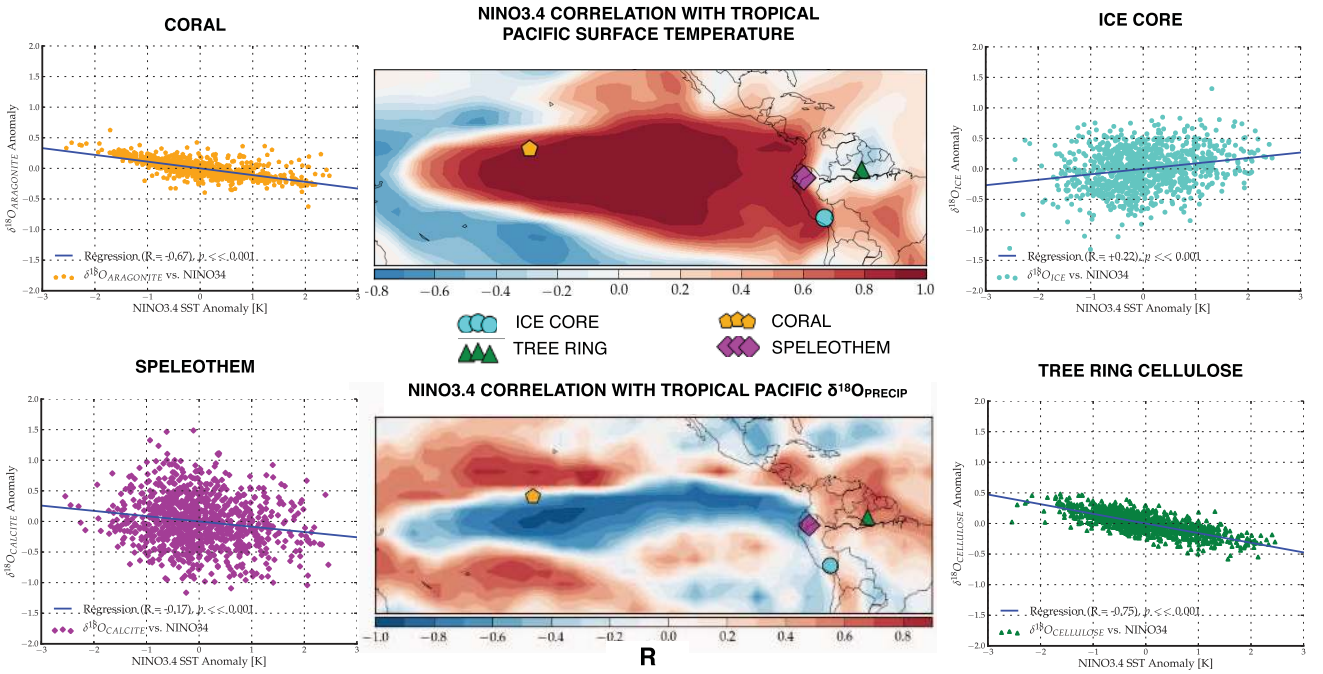

Figure 11. Using PRYSM to simulate multi-proxy networks: how do four different proxy types capture different aspects of ENSO across the tropical Pacific? The figure shows the spatial correlation of tropical Pacific temperatures (top map) and $\delta^{18}O_P$ (bottom map) and the NINO3.4 SST index. Four proxy types at four different locations (colored dots on the map) each uniquely filter the input climate signal. The regression of simulated $\delta^{18}O$ (using SPEEDY-IER and the PSM sensor models) for each proxy system (a coral from Palmyra island, a speleothem record in Ecuador, a tree-ring cellulose record from Amazonia, and an ice core record from the Andes) against NINO3.4 SST anomalies is shown in the four corner plots.

the climate signal is robust in the proxy's response, while an SNR closer to zero is indicative of lower quality. All of the pseudoproxies exhibit a significant correlation with NINO3.4 SSTs at the sensor level, on both annual and decadal timescales. The strength of the captured climate signal varies by proxy type, with tree rings and corals offering the highest fidelity in sensing ENSO variability. As higher-order uncertainties are applied through the archive and observation models, however, the resulting signal loses strength. At both annual and decadal resolution, the ice core loses signal information as a result of diffusion and compaction down core (quantified via the archive model). Further, based on the (2.5% and 97.5%) highest-density region (HDR) of the ensemble of 1000 age-perturbed realizations, each proxy suffers a large reduction in captured signal strength given imposed dating uncertainties ("full-psm" values); in many cases, the relationship can vanish or change direction. Finally, when both the climate (NINO3.4) and the proxy signals are smoothed to decadal resolution (bottom

Table 6. Correlation Between Proxy Data and ENSO (R) and Signal-to-Noise Ratios (SNR) at Annual and Decadal Scales for the Four Proxy Types[a]

		R			SNR		
	Proxy Class	Sensor	Sensor+ Archive	Full PSM	Sensor	Sensor+ Archive	Full PSM
Annual	Tree Cellulose	**−0.75**		$_{-0.26}\mathbf{-0.07}_{+0.06}$	*1.13*		$_{0.27}0.07_{0.06}$
	Ice Core	**+0.22**	0.03	$_{+0.01}+0.03_{+0.06}$	*0.23*	*0.03*	$_{0.01}0.03_{0.06}$
	Coral	**−0.67**		$_{-0.33}\mathbf{-0.09}_{+0.04}$	*0.90*		$_{0.35}0.09_{0.04}$
	Speleothem	**−0.17**		$_{-0.09}-0.03_{+0.03}$	*0.17*		$_{0.09}0.03_{0.03}$
Decadal	Tree Cellulose	**−0.63**		$_{-0.57}\mathbf{-0.38}_{-0.17}$	*0.80*		$_{0.68}0.41_{0.17}$
	Ice Core	**+ 0.40**	0.09	$_{+0.07}+0.10_{+0.16}$	*0.43*	*0.09*	$_{0.07}0.09_{0.16}$
	Coral	**−0.70**		$_{-0.66}\mathbf{-0.50}_{-0.27}$	*0.98*		$_{0.89}0.59_{0.28}$
	Speleothem	**−0.36**		$_{-0.25}-0.14_{-0.02}$	*0.38*		$_{0.26}0.14_{0.02}$

[a]R and SNR are reported after the input climate signal is altered by the sensor, archive, and observation models in succession. Statistical significance at the 5% level (as judged by a *t* test accounting for the autocorrelation of each series) is indicated in bold. The observation model regression values are drawn from an ensemble of 1000 age realizations with imposed dating uncertainties (2% for ice cores, 3% for corals, and 4% for tree-ring cellulose, all with symmetric miscounting rates. Speleothem age uncertainties were generated with Bchron using 20 dates assuming a 60 cm core). We then generated 100 additional realizations accounting for analytical uncertainty (*y* axis) by adding Gaussian white noise given an instrumental or measurement error of 0.1‰ to each of the 1000 age-perturbed realizations. Numbers of the form $_{2.5\%}50\%_{97.5\%}$ represent, respectively, the 2.5%, 50% and 97.5% quantiles of the simulated ensemble.

half of Table 6), the ice core and speleothem SNRs roughly double; however, age uncertainties may lower the SNR to the point that they are no longer informative of NINO3.4, as is the case in this particular example. This type of simulation would serve to motivate better age control (e.g., through replication) to enhance the SNR and hence the value of a record to a multiproxy reconstruction.

As expected, precisely dated proxies like the tree ring and coral shown here exhibit stronger signals on decadal timescales. This illustrates how smoothing may offset random age errors. In this example, age errors for the speleothem are too large for this strategy to work on decadal scales, but this framework would allow one to determine how many dates are needed, and how precise they should be, for the speleothem record to be informative of NINO3.4 SST at a given time scale.

We note that the SNR values simulated here may be lower than observed in published paleoclimate data sets. Clearly, the caveats described in sections 4.1–4.3 (structural and parametric errors in the PSMs, as well as uncertainties in the input signal) apply *a fortiori* in a multiproxy context. Multi-sensor, archive and observational replication, smoothing, integration and expert choices made in site selection, data acquisition, and data analysis may give rise to SNRs larger in nature than simulated here; however, because the submodels mimic proxy system processes which should not be ignored, this builds intuition about the interpretation of climate reconstructions (especially for extrapolations in time, space, and frequency).

In spite of these caveats, the data given in Table 6 demonstrate the utility of our modeling framework for generating a process-based estimate of the SNR, accounting for differences between each proxy system. In this way, PSMs offer a framework to generate more realistic pseudoproxy networks (*Evans et al.*, 2014] spanning multiple proxy types for a given region. Such PSM-generated PPEs will improve multiproxy network interpretation by allowing to explore how a climate signal is mediated by a broad, multiproxy network of paleoclimate observations.

5. Discussion and Future Work

This study gathers intermediate complexity models for four oxygen isotope-based proxy systems (coral aragonite, tree ring cellulose, speleothem calcite, and ice cores). The result, PRYSM, offers a unified and compartmentalized framework for proxy system modeling. This paper serves two purposes: (1) demonstrate the types of scientific insights that may be generated by coupling such proxy models together, and to GCMs; (2) integrate what were heretofore separate models in a common, open-source framework.

The integration of proxy system submodels (sensor, archive, observation) allows one to fingerprint the principal environmental controls on paleoclimate observations, and thus can be used to refine the interpretation of proxy records. Leveraging this compartmentalization, one can track the evolution of the original climate signal and map the propagation of errors through each transformation. Navigating this framework highlights gaps in the understanding of proxy systems, and encourages a more rigorous analysis of uncertainties where those gaps appear. For example, we showed that uncertain physical model parameters may fundamentally alter the shape of proxy-derived spectra, confounding the interpretation of low frequency variability in such records (section 4.1). Modeling ice cores using different GCM output allowed us to quantify the effects of diffusion and compaction, and to explore the challenges faced by data-model comparison (section 4.2). The PSM framework can be used to simulate an ensemble of realizations for a full multiproxy network, all drawn from an age distribution under assumed dating and analytical uncertainties. We showed how realistic age errors may lower the ability of a proxy network to capture a common climate signal (section 4.3). Finally, PRYSM lends insight into how different proxy types filter a common climate signal, and can be used to generate realistic, proxy and site-specific estimates of the SNR (section 4.4). In particular, the PSM framework facilitates multiproxy PPEs, and can identify difficulties that may arise combining multiple time-uncertain records across different proxy types.

In all these applications, PRYSM provides a simulator for error quantification. Further, PRYSM's modularity facilitates an estimate of structural uncertainty, as different submodels can be implemented interchangeably to diagnose their influence on the final signal. Parametric uncertainties, on the other hand, may be estimated by varying PSM parameters for environmental or geochemical variables (e.g., groundwater transit time or miscounting rate) and quantifying the total change to the final signal. In the past, those parameters have often been hardwired, but PRYSM makes it easy to specify alternate values; this is critical in Bayesian applications, where such values are drawn from a distribution. We find that when applied via the submodel context,

analytical errors may be inconsequential as compared to other sources of uncertainty. While analytical errors are often the main uncertainty reported alongside paleoclimate observations, our analysis suggests that it may be more important to consider dating uncertainties, for example.

The coupling of PSMs with isotope-enabled GCMs enhances the utility of isotopic paleoclimate data for validating predictive climate models. While caution is needed for making sound comparisons between simulated paleoclimate data and observations, PRYSM enables a more direct "apples to apples" comparison between simulated paleoclimate data driven with GCM environmental variables and actual observations (section 4.2). These comparisons allow one to more finely diagnose the origin of model-data discrepancies, helping to identify problems that may arise from nonlinearities in proxy-climate relationships, GCM shortcomings, or the presence of age uncertainties, for example. Within the combined GCM+PSM framework, it may often prove difficult to isolate and/or abate structural and parametric error contributions from either model simulations and forward modeled data (section 4.2). Different GCMs may harbor distinct biases, and a loss of spatial precision due to the coarse resolution of model grids limits the investigative utility of this method. Still, GCMs with water isotope physics schemes allow us to check the validity of elemental assumptions, (e.g., the parameterization of $\delta^{18}O_{seawater}$ by SSS in corals, as done in *Russon et al.* [2013]), and lend insight into the dynamical causes of site-specific variability in precipitation isotope ratios (moisture source or "amount effect") [e.g., *Risi et al.*, 2008].

There are inherent caveats to the forward modeling approach. In many cases, the PSMs represent a large simplification to complex geochemical systems, and may fail to capture important processes. This is especially true for biological systems. Our design choices were guided by two main considerations: (a) the state of knowledge on a particularly proxy, as represented by the literature and/or existing PSMs; and (b) the availability of high-quality observations to constrain the PSMs. In general, the PSM application is limited by the quality of the input, structural and parameter estimations that comprise the simulations. Indeed, modeling such processes necessitates the introduction of parameters that may or may not be well constrained by observations, and the required validation data are not always available. In a sense, the availability (or lack thereof) of high-quality observations limits the allowable PSM complexity. We thus have employed only first-order models to avoid significant assumptions regarding parameters that cannot currently be constrained via process study or observation. As this knowledge expands, we expect that it will be possible (indeed, necessary) to shift this frontier toward more complexity. Models are only as good as the observations they are based on, and we hope that PRYSM's simplicity will spur the collection of more detailed data sets for proxy ground-truthing and modeling (as done, for instance, by *Moerman et al.* [2014] and *Noone et al.* [2014]).

For the first iteration of this package, we have focused on water isotope-based proxies with high-resolution applications. In the near future, we plan to refine current models (e.g., by including more detailed models for ice core diffusion and karst systems) and expand to a broader class of proxies. Conspicuously absent are proxies based on ocean and lake sediments; we plan to include sedimentary archives, taking into account the effects of sedimentation and bioturbation) and sensors such as leaf wax δD and planktonic foramnifera $\delta^{18}O$.

Through these extensions, we hope to provide more detailed investigations of each proxy system, and lend insight into the mechanisms whereby proxies record climate. The framework will be used for optimal network design (M. Comboul et al., accepted 2014), to design more realistic pseudo-proxy experiments [*Evans et al.*, 2014], for paleoclimate state estimation [*Bhend et al.*, 2012; *Steiger et al.*, 2014] or as the data level in Bayesian hierarchical models [*Tolwinski-Ward et al.*, 2013; *Tingley et al.*, 2012]. PRYSM may also help motivate further process studies for proxy systems, improving our interpretations of paleoclimate observations on site-by-site and network bases. Finally, PRYSM offers the potential for improving the utility of multi-proxy data sets by breaking down the relative contributions to the total systematic error over time given changes in the observing network, data type, and varying chronological uncertainty.

This modeling framework provides a new computational tool for the paleoclimate community, adaptable and designed to facilitate modular changes concurrent with advances in process-based studies for proxy systems. In the long term, we envision extending this framework to encompass the majority of paleoclimate observations, regardless of resolution. We invite external contributions via a GitHub repository https://github.com/sylvia-dee/PRYSM, and hope that this initial effort will serve as a cornerstone for progress in paleoclimatology, stimulating community-sourced PSM development, collaborations between climate modelers and paleoclimate field scientists, and building capacity at the community level.

Acknowledgments
This work was supported by NOAA Climate Change Data and Detection grants NA10OAR4310115 and NA10OAR4310116, as well as NOAA Climate Program Office grant NA14OAR4310175. The code described in this manuscript, and which can be used to reproduce our results, is available at https://github.com/sylvia-dee/PRYSM. SGD thanks Nathan Steiger for help accessing ECHAM5-wiso model output, and Jessica Moerman, Nick Scroxton, Jud Partin, Tas van Ommen, Vasileios Gkinis, and Bronwen Konecky for their helpful guidance in developing PSMs and support in furthering this project. JEG thanks James W. Kirchner and Jordan F. Clark for illuminating discussions on catchment hydrochemistry. Many thanks to Julia Tindall and the additional reviewers for their helpful feedback.

References

Alley, R. B., et al. (1997), Visual-stratigraphic dating of the GISP2 ice core: Basis, reproducibility, and application, *J. Geophys. Res.*, *102*, 26,367–26,381, doi:10.1029/96JC03837.

Anchukaitis, K. J., and J. E. Tierney (2013), Identifying coherent spatiotemporal modes in time-uncertain proxy paleoclimate records, *Clim. Dyn.*, *41*(5-6), 1291–1306, doi:10.1007/s00382-012-1483-0.

Anchukaitis, K. J., M. N. Evans, A. Kaplan, E. A. Vaganov, M. K. Hughes, H. D. Grissino-Mayer, and M. A. Cane (2006), Forward modeling of regional scale tree-ring patterns in the southeastern United States and the recent influence of summer drought, *Geophys. Res. Lett.*, *33*, L04705, doi:10.1029/2005GL025050.

Anderson, W., S. Bernasconi, J. McKenzie, M. Saurer, and F. Schweingruber (2002), Model evaluation for reconstructing the oxygen isotopic composition in precipitation from tree ring cellulose over the last century, *Chem. Geol.*, *182*(2-4), 121–137, doi:10.1016/S0009-2541(01)00285-6.

Arthern, R. J., D. G. Vaughan, A. M. Rankin, R. Mulvaney, and E. R. Thomas (2010), In situ measurements of Antarctic snow compaction compared with predictions of models, *J. Geophys. Res. Earth Surf.*, *115*, F03011, doi:10.1029/2009JF001306.

Ault, T. R., J. E. Cole, J. T. Overpeck, G. T. Pederson, S. St. George, B. Otto-Bliesner, C. A. Woodhouse, and C. Deser (2013a), The continuum of hydroclimate variability in western North America during the last millennium, *J. Clim.*, *26*(16), 5863–5878, doi:10.1175/JCLI-D-11–00732.1.

Ault, T. R., C. Deser, M. Newman, and J. Emile-Geay (2013b), Characterizing decadal to centennial variability in the equatorial pacific during the last millennium, *Geophys. Res. Lett.*, *40*, 3450–3456, doi:10.1002/grl.50647.

Bader, H. (1954), Sorges law of densification of snow on high polar glaciers, *J. Glaciol*, *2*(15), 319–323.

Baker, A., and C. Bradley (2010), Modern stalagmite δ18O: Instrumental calibration and forward modelling, *Global Planet. Change*, *71*(3-4), 201–206, doi:10.1016/j.gloplacha.2009.05.002.

Baker, A., C. Bradley, S. Phipps, M. Fischer, I. Fairchild, L. Fuller, C. Spötl, and C. Azcurra (2012), Millennial-length forward models and pseudoproxies of stalagmite δ^{18}O: An example from NW Scotland, *Clim. Past*, *8*(4), 1153–1167, doi:10.5194/cp-8–1153-2012.

Baker, A. J., D. P. Mattey, and J. U. Baldini (2014), Reconstructing modern stalagmite growth from cave monitoring, local meteorology, and experimental measurements of dripwater films, *Earth Planet. Sci. Lett.*, *392*, 239–249, doi:10.1016/j.epsl.2014.02.036.

Baldini, J., F. McDermott, and I. Fairchild (2006), Spatial variability in cave drip water hydrochemistry: Implications for stalagmite paleoclimate records, *Chem. Geol.*, *235*(3), 390–404, doi:10.1016/j.chemgeo.2006.08.005.

Barbour, M. M., J. S. Roden, G. D. Farquhar, and J. R. Ehleringer (2004), Expressing leaf water and cellulose oxygen isotope ratios as enrichment above source water reveals evidence of a Péclet effect, *Oecologia*, *138*(3), 426–435, doi:10.1007/s00442-003-1449-3.

Beck, J. W., et al. (2001), Extremely large variations of atmospheric 14C concentration during the last glacial period, *Science*, *292*(5526), 2453–2458, doi:10.1126/science.1056649.

Bhend, J., J. Franke, D. Folini, M. Wild, and S. Brönnimann (2012), An ensemble-based approach to climate reconstructions, *Clim. Past*, *8*(3), 963–976, doi:10.5194/cp-8–963-2012.

Blaauw, M. (2010), Methods and code for 'classical' age-modelling of radiocarbon sequences, *Quat. Geochronol.*, *5*(5), 512–518, doi:10.1016/j.quageo.2010.01.002.

Blaauw, M., and J. A. Christen (2005), Radiocarbon peat chronologies and environmental change, *J. R. Stat. Soc., Ser. C*, *54*(4), 805–816, doi:10.1111/j.1467–9876.2005.00516.x.

Blaauw, M., and J. A. Christen (2011), Flexible paleoclimate age-depth models using an autoregressive gamma process, *Bayesian Anal.*, *6*(3), 457–474, doi:10.1214/11-BA618.

Bradley, C., A. Baker, C. N. Jex, and M. J. Leng (2010), Hydrological uncertainties in the modelling of cave drip-water δ^{18}O and the implications for stalagmite palaeoclimate reconstructions, *Quat. Sci. Rev.*, *29*(17), 2201–2214, doi:10.1016/j.quascirev.2010.05.017.

Braganza, K., J. L. Gergis, S. B. Power, J. S. Risbey, and A. M. Fowler (2009), A multiproxy index of the, a.d. 1525–1982, *J. Geophys. Res.*, *114*, D05106, doi:10.1029/2008JD010896.

Breitenbach, S. F. M., et al. (2012), Constructing proxy records from age models (copra), *Clim. Past*, *8*, 1765–1779, doi:10.5194/cp-8–1765-2012.

Brienen, R. J. W., G. Helle, T. L. Pons, J.-L. Guyot, and M. Gloor (2012), Oxygen isotopes in tree rings are a good proxy for Amazon precipitation and El Niño-Southern Oscillation variability, *Proc. Natl. Acad. Sci. U. S. A.*, *109*(42), 16,957–16,962, doi:10.1073/pnas.1205977109.

Bronk-Ramsey, C. (1995), Radiocarbon calibration and analysis of stratigraphy: The OxCal program, *Radiocarbon*, *37*(2), 425–430.

Bronk-Ramsey, C. (2008), Deposition models for chronological records, *Quat. Sci. Rev.*, *27*(1), 42–60, doi:10.1016/j.quascirev.2007.01.019.

Bronk-Ramsey, C. (2009), Bayesian analysis of radiocarbon dates, *Radiocarbon*, *51*(1), 337–360.

Brönnimann, S., I. Mariani, M. Schwikowski, R. Auchmann, and A. Eichler (2012), Simulating the temperature and precipitation signal in an Alpine ice core, *Clim. Past Discuss.*, *8*, 6111–6134, doi:10.5194/cpd-8–6111-2012.

Burgess, P. M., and V. P. Wright (2003), Numerical forward modeling of carbonate platform dynamics: An evaluation of complexity and completeness in carbonate strata, *J. Sediment. Res.*, *73*(5), 637–652.

Capron, E., et al. (2013), Glacial–interglacial dynamics of Antarctic firn columns: Comparison between simulations and ice core air-δ15N measurements, *Clim. Past*, *9*(3), 983–999, doi:10.5194/cp-9-983-2013.

Cole, J. E., and R. G. Fairbanks (1990), The Southern Oscillation recorded in the of corals from Tarawa Atoll, *Paleoceanography*, *5*, 669–683.

Comboul, M., J. Emile-Geay, M. Evans, N. Mirnateghi, K. M. Cobb, and D. M. Thompson (2014), A probabilistic model of chronological errors in layer-counted climate proxies: Applications to annually banded coral archives, *Clim. Past*, *10*(2), 825–841, doi:10.5194/cp-10-825-2014.

Corrège, T. (2006), Sea surface temperature and salinity reconstruction from coral geochemical tracers, *Palaeogeogr. Palaeoclimatol. Palaeoecol.*, *232*(2–4), 408–428, doi:10.1016/j.palaeo.2005.10.014.

Craig, H., and L. I. Gordon (1965), Deuterium and Oxygen-18 variations in the ocean and the marine atmosphere, in *Proceedings of Stable Isotopes in Oceanography Studies and Paleotemperatures*, pp. 9–130, Lab. Geol. Nucl., Pisa, Italy.

Cuffey, K. M., and E. J. Steig (1998), Isotopic diffusion in polar firn: Implications for interpretation of seasonal climate parameters in ice-core records, with emphasis on central Greenland, *J. Glaciol.*, *44*(147), 273–284.

Dansgaard, W. (1964), Stable isotopes in precipitation, *Tellus*, *16*(4), 436–468.

Dee, S. (2013), Refining the interpretation of hydroclimate paleodata via the integration of an isotope-enabled agcm and proxy system models, Abstract PP23C-1990 presented at 2013 AGU Fall Meeting, AGU, San Francisco, Calif.

Dee, S., J. Emile-Geay, M. Evans, and D. Noone (2014a), Comparing apples to apples: Paleoclimate model-data comparison via proxy system modeling, in *EGU General Assembly Conference Abstracts, 16*, 9636.

Dee, S., D. Noone, N. Buenning, J. Emile-Geay, and Y. Zhou (2014b), SPEEDY-IER: A fast atmospheric GCM with water isotope physics, *J. Geophys. Res. Atmos.*, *120*, 73–91, doi:10.1002/2014JD022194.

Delcroix, T., G. Alory, Corrège, and M. J. McPhaden (2011), A gridded sea surface salinity data set for the tropical Pacific with sample applications (1950–2008), *Deep Sea Res., Part I*, *58*, 38–48, doi:10.1016/j.dsr.2010.11.002.

DeLong, K. L., T. M. Quinn, F. W. Taylor, C.-C. Shen, and K. Lin (2013), Improving coral-base paleoclimate reconstructions by replicating 350 years of coral sr/ca variations, *Palaeogeogr. Palaeoclimatol. Palaeoecol.*, *373*, 6–24, doi:10.1016/j.palaeo.2012.08.019.

Dreybrodt, W., and D. Scholz (2011), Climatic dependence of stable carbon and oxygen isotope signals recorded in speleothems: From soil water to speleothem calcite, *Geochim. Cosmochim. Acta*, *75*(3), 734–752, doi:10.1016/j.gca.2010.11.002.

Drysdale, R. N., G. Zanchetta, J. C. Hellstrom, A. E. Fallick, and J.-X. Zhao (2005), Stalagmite evidence for the onset of the last interglacial in southern Europe at 129±1 ka, *Geophys. Res. Lett.*, *32*, L24708, doi:10.1029/2005GL024658.

Emile-Geay, J., K. Cobb, M. Mann, and A. T. Wittenberg (2013a), Estimating Central Equatorial Pacific SST variability over the past millennium. Part 1: Methodology and validation, *J. Clim.*, *26*, 2302–2328, doi:10.1175/JCLI-D-11-00510.1.

Emile-Geay, J., K. Cobb, M. Mann, and A. T. Wittenberg (2013b), Estimating Central Equatorial Pacific SST variability over the past millennium. Part 2: Reconstructions and implications, *J. Clim.*, *26*, 2329–2352, doi:10.1175/JCLI-D-11–00511.1.

Epstein, S., R. Buchsbaum, H. A. Lowenstam, and H. C. Urey (1953), Revised carbonate-water isotopic temperature scale, *Geol. Soc. Am. Bull.*, *64*(11), 1315–1326.

Evans, M., S. Tolwinski-Ward, D. Thompson, and K. Anchukaitis (2013), Applications of proxy system modeling in high resolution paleoclimatology, *Quat. Sci. Rev.*, *76*, 16–28, doi:10.1016/j.quascirev.2013.05.024.

Evans, M., J. Smerdon, A. Kaplan, S. Tolwinski-Ward, and J. González-Rouco (2014), Climate field reconstruction uncertainty arising from multivariate and nonlinear properties of predictors, *Geophys. Res. Lett.*, *41*, 9127–9134, doi:10.1002/2014GL062063.

Evans, M. N. (2007), Toward forward modeling for paleoclimatic proxy signal calibration: A case study with oxygen isotopic composition of tropical woods, *Geochem. Geophys. Geosyst.*, *8*, Q07008, doi:10.1029/2006GC001406.

Evans, M. N., and D. P. Schrag (2004), A stable isotope-based approach to tropical dendroclimatology, *Geochim. Cosmochim. Acta*, *68*(16), 3295–3305, doi:10.1016/j.gca.2004.01.006.

Evans, M. N., A. Kaplan, and M. A. Cane (2000), Intercomparison of coral oxygen isotope data and historical sea surface temperature (SST): Potential for coral-based SST field reconstructions, *Paleoceanography*, *15*, 551–563, doi:10.1029/2000PA000498.

Evans, M. N., B. K. Reichert, a. Kaplan, K. J. Anchukaitis, E. a. Vaganov, M. K. Hughes, and M. a. Cane (2006), A forward modeling approach to paleoclimatic interpretation of tree-ring data, *J. Geophys. Res.*, *111*, G03008, doi:10.1029/2006JG000166.

Fairbanks, R. G., M. N. Evans, J. L. Rubenstone, R. A. Mortlock, K. Broad, M. D. Moore, and C. D. Charles (1997), Evaluating climate indices and their geochemical proxies measured in corals, *Coral Reefs*, *16*(1), S93–S100, doi:10.1007/s003380050245.

Fairchild, I. J., C. L. Smith, A. Baker, L. Fuller, C. Spötl, D. Mattey, and F. McDermott (2006a), Modification and preservation of environmental signals in speleothems, *Earth Sci. Rev.*, *75*(1), 105–153.

Fairchild, I. J., G. W. Tuckwell, A. Baker, and A. F. Tooth (2006b), Modelling of dripwater hydrology and hydrogeochemistry in a weakly karstified aquifer (Bath, UK): Implications for climate change studies, *J. Hydrol.*, *321*(1), 213–231.

Gagan, M. K., L. K. Ayliffe, J. W. Beck, J. E. Cole, E. R. M. Druffel, R. B. Dunbar, and D. P. Schrag (2000), New views of tropical paleoclimates from corals, *Quat. Sci. Rev.*, *19*(1–5), 45–64, doi:10.1016/S0277-3791(99)00054-2.

Gelhar, L. W., and J. L. Wilson (1974), Ground-water quality modelinga, *Groundwater*, *12*(6), 399–408.

Genty, D., et al. (2006), Timing and dynamics of the last deglaciation from European and North African δ^{13}C stalagmite profiles—Comparison with Chinese and South Hemisphere stalagmites, *Quat. Sci. Rev.*, *25*(17–18), 2118–2142, doi:10.1016/j.quascirev.2006.01.030.

Gkinis, V., S. Simonsen, S. Buchardt, J. White, and B. Vinther (2014), Water isotope diffusion rates from the NorthGRIP ice core for the last 16,000 years glaciological and paleoclimatic implications, *Earth Planet. Sci. Lett.*, *405*, 132–141, doi:10.1016/j.epsl.2014.08.022.

Godsey, S. E., et al. (2010), Generality of fractal 1/f scaling in catchment tracer time series, and its implications for catchment travel time distributions, *Hydrol. Processes*, *24*(12), 1660–1671, doi:10.1002/hyp.7677.

Goujon, C., J.-M. Barnola, and C. Ritz (2003), Modeling the densification of polar firn including heat diffusion: Application to close-off characteristics and gas isotopic fractionation for Antarctica and Greenland sites, *J. Geophys. Res.*, *108*(D24), 4792, doi:10.1029/2002JD003319.

Grossman, E. L., and T.-L. Ku (1986), Oxygen and carbon isotope fractionation in biogenic aragonite: Temperature effects, *Chem. Geol.*, *59*, 59–74.

Hall, W., and H. Pruppacher (1976), The survival of ice particles falling from cirrus clouds in subsaturated air, *J. Atmos. Sci.*, *33*(10), 1995–2006.

Hartmann, A., J. A. Barberà, J. Lange, B. Andreo, and M. Weiler (2013), Progress in the hydrologic simulation of time variant recharge areas of karst systems—Exemplified at a karst spring in southern Spain, *Adv. Water Resour.*, *54*, 149–160, doi:10.1016/j.advwatres.2013.01.010.

Haslett, J., and A. Parnell (2008), A simple monotone process with application to radiocarbon-dated depth chronologies, *J. R. Stat. Soc. Ser. C*, *57*(4), 399–418, doi:10.1111/j.1467-9876.2008.00623.x.

Heegaard, E., H. J. B. Birks, and R. J. Telford (2005), Relationships between calibrated ages and depth in stratigraphical sequences: An estimation procedure by mixed-effect regression, *Holocene*, *15*(4), 612–618, doi:10.1191/0959683605hl836rr.

Hendy, E. J., P. J. Tomiak, M. J. Collins, J. Hellstrom, A. W. Tudhope, J. M. Lough, and K. E. Penkman (2012), Assessing amino acid racemization variability in coral intra-crystalline protein for geochronological applications, *Geochim. Cosmochim. Acta*, *86*, 338–353.

Herron, M. M., and C. C. Langway (1980), Firn densification: An empirical model, *J. Glaciol.*, *25*, 373–385.

Hoffmann, D. L., J. W. Beck, D. A. Richards, P. L. Smart, J. S. Singarayer, T. Ketchmark, and C. J. Hawkesworth (2010), Towards radiocarbon calibration beyond 28ka using speleothems from the Bahamas, *Earth Planet. Sci. Lett.*, *289*(1), 1–10, doi:10.1016/j.epsl.2009.10.004.

Johnsen, S. J. (1977), Stable isotope homogenization of polar firn and ice, in *Proceedings of the Symposium on Isotopes and Impurities in Snow and Ice, IAHS–AISH Publ. 118*, pp. 210–219, Int. Assoc. of Hydrol. Sci., Gentbrugge, Belgium.

Johnsen, S. J., H. B. Clausen, K. M. Cuffey, G. Hoffmann, J. Schwander, and T. Creyts (2000), Diffusion of stable isotopes in polar firn and ice: The isotope effect in firn diffusion, *Phys. Ice Core Records*, *159*, 121–140.

Kaufmann, G., and W. Dreybrodt (2004), Stalagmite growth and palaeo-climate: An inverse approach, *Earth Planet. Sci. Lett.*, *224*(3), 529–545.

Kirchner, J. W., X. Feng, and C. Neal (2001), Catchment-scale advection and dispersion as a mechanism for fractal scaling in stream tracer concentrations, *J. Hydrol.*, *254*(1–4), 82–101, doi:10.1016/S0022-1694(01)00487-5.

Klauenberg, K., P. G. Blackwell, C. E. Buck, R. Mulvaney, R. Röthlisberger, and E. W. Wolff (2011), Bayesian glaciological modelling to quantify uncertainties in ice core chronologies, *Quat. Sci. Rev.*, *30*(21), 2961–2975, doi:10.1016/j.quascirev.2011.03.008.

Klaus, J., and J. McDonnell (2013), Hydrograph separation using stable isotopes: Review and evaluation, *J. Hydrol.*, *505*, 47–64, doi:10.1016/j.jhydrol.2013.09.006.

Küttel, M., E. J. Steig, Q. Ding, A. J. Monaghan, and D. S. Battisti (2012), Seasonal climate information preserved in West Antarctic ice core water isotopes: Relationships to temperature, large-scale circulation, and sea ice, *Clim. Dyn.*, *39*(7-8), 1841–1857.

Landrum, L., B. L. Otto-Bliesner, E. R. Wahl, A. Conley, P. J. Lawrence, N. Rosenbloom, and H. Teng (2013), Last millennium climate and its variability in CCSM4, *J. Clim.*, *26*(4), 1085–1111, doi:10.1175/JCLI-D-11–00326.1.

Lee, J.-E., I. Fung, D. J. DePaolo, and C. C. Henning (2007), Analysis of the global distribution of water isotopes using the NCAR atmospheric general circulation model, *J. Geophys. Res.*, *112*, D16306, doi:10.1029/2006JD007657.

LeGrande, A. N., and G. a. Schmidt (2006), Global gridded data set of the oxygen isotopic composition in seawater, *Geophys. Res. Lett.*, *33*, L12604, doi:10.1029/2006GL026011.

Li, J., and H. J. Zwally (2011), Modeling of firn compaction for estimating ice-sheet mass change from observed ice-sheet elevation change, *Ann. Glaciol.*, *52*(59), 1–7, doi:10.3189/172756411799096321.

Lough, J. (2004), A strategy to improve the contribution of coral data to high-resolution paleoclimatology, *Palaeogeogr. Palaeoclimatol. Palaeoecol.*, *204*(1), 115–143, doi:10.1016/S0031-0182(03)00727-2.

Lough, J. M. (2010), Climate records from corals, *Clim. Change*, *1*(3), 318–331, doi:10.1002/wcc.39.

Lyons, R. P., C. N. Kroll, and C. A. Scholz (2011), An energy-balance hydrologic model for the Lake Malawi Rift Basin, East Africa, *Global Planet. Change*, *75*(1), 83–97, doi:10.1016/j.gloplacha.2010.10.010.

Mann, M. E., and S. Rutherford (2002), Climate reconstruction using pseudoproxies, *Geophys. Res. Lett.*, *29*(10), 1501, doi:10.1029/2001GL014554.

Mathieu, R., D. Pollard, J. E. Cole, J. W. White, R. S. Webb, and S. L. Thompson (2002), Simulation of stable water isotope variations by the GENESIS GCM for modern conditions, *J. Geophys. Res.*, *107*(D4), 4037, doi:10.1029/2001JD900255.

McCarroll, D., and N. J. Loader (2004), Stable isotopes in tree rings, *Quat. Sci. Rev.*, *23*(7), 771–801, doi:10.1016/j.quascirev.2003.06.017.

McDermott, F. (2004), Palaeo-climate reconstruction from stable isotope variations in speleothems: A review, *Quat. Sci. Rev.*, *23*(7), 901–918, doi:10.1016/j.quascirev.2003.06.021.

McDonnell, J. J. (1990), A rationale for old water discharge through macropores in a steep, humid catchment, *Water Resour. Res.*, *26*, 2821–2832,.

McGuire, K. J., and J. J. McDonnell (2006), A review and evaluation of catchment transit time modeling, *J. Hydrol.*, *330*(3–4), 543–563, doi:10.1016/j.jhydrol.2006.04.020.

Moerman, J. W., K. M. Cobb, J. W. Partin, A. N. Meckler, S. A. Carolin, J. F. Adkins, S. Lejau, J. Malang, B. Clark, and A. A. Tuen (2014), Transformation of ENSO-related rainwater to dripwater variability by vadose water mixing, *Geophys. Res. Lett.*, *41*, 7907–7915, doi:10.1002/2014GL061696.

Mühlinghaus, C., D. Scholz, and A. Mangini (2009), Modelling fractionation of stable isotopes in stalagmites, *Geochim. Cosmochim. Acta*, *73*(24), 7275–7289, doi:10.1016/j.gca.2009.09.010.

Noone, D., A. Raudzens-Bailey, M. Berkelhammer, C. Cox, K. Steffen, and J. White (2014), A reassessment of Greenland climate history using a proxy system model for accumulation of the isotope record in snow, Abstract PP34B-07 presented at 2014 AGU Fall Meeting, AGU, San Francisco, Calif.

O'Neil, J. R., R. N. Clayton, and T. K. Mayeda (1969), Oxygen isotope fractionation in divalent metal carbonates, *J Chem. Phys.*, *51*(12), 5547–5558.

Parnell, A. C., C. E. Buck, and T. K. Doan (2011a), A review of statistical chronology models for high-resolution, proxy-based holocene palaeoenvironmental reconstruction, *Quat. Sci. Rev.*, *30*(21–22), 2948–2960, doi:10.1016/j.quascirev.2011.07.024.

Parnell, A. C., C. E. Buck, and T. K. Doan (2011b), A review of statistical chronology models for high-resolution, proxy-based holocene palaeoenvironmental reconstruction, *Quat. Sci. Rev.*, *30*(21), 2948–2960.

Partin, J. W., et al. (2013), Multidecadal rainfall variability in South Pacific Convergence Zone as revealed by stalagmite geochemistry, *Geology*, *41*(11), 1143–1146, doi:10.1130/G34718.1.

Polyak, V. J., and Y. Asmerom (2001), Late Holocene Climate and Cultural Changes in the Southwestern United States, *Science*, *294*(5540), 148–151, doi:10.1126/science.1062771.

Polyak, V. J., J. C. Cokendolpher, R. A. Norton, and Y. Asmerom (2001), Wetter and cooler late Holocene climate in the southwestern United States from mites preserved in stalagmites, *Geology*, *29*(7), 643–646.

Polyak, V. J., J. B. Rasmussen, and Y. Asmerom (2004), Prolonged wet period in the southwestern United States through the Younger Dryas, *Geology*, *32*(1), 5–8, doi:10.1130/G19957.1.

Risi, C., S. Bony, and F. Vimeux (2008), Influence of convective processes on the isotopic composition ($\delta^{18}O$ and δD) of precipitation and water vapor in the tropics: 2. Physical interpretation of the amount effect, *J. Geophys. Res.*, *113*, D19306, doi:10.1029/2008JD009943.

Roden, J. S., and J. R. Ehleringer (1999), Hydrogen and oxygen isotope ratios of tree-ring cellulose for riparian trees grown long-term under hydroponically controlled environments, *Oecologia*, *121*(4), 467–477.

Roden, J. S., G. Lin, and J. R. Ehleringer (2000), A mechanistic model for interpretation of hydrogen and oxygen isotope ratios in tree-ring cellulose, *Geochim. Cosmochim. Acta*, *64*(1), 21–35.

Roden, J. S., G. Lin, and J. R. Ehleringer (2002), Response to the comment of V.J. Terwilliger on "A mechanistic model for interpretation of hydrogen and oxygen ratios in tree-ring cellulose", by J. S. Roden, G. Lin, and J. R. Ehleringer (2000), *Geochim. Cosmochim. Acta*, *66*, 733–734.

Romanov, D., G. Kaufmann, and W. Dreybrodt (2008), Modeling stalagmite growth by first principles of chemistry and physics of calcite precipitation, *Geochim. Cosmochim. Acta*, *72*(2), 423–437, doi:10.1016/j.gca.2007.09.038.

Russon, T., A. W. Tudhope, G. C. Hegerl, M. Collins, and J. Tindall (2013), Inter-annual tropical Pacific climate variability in an isotope-enabled CGCM: Implications for interpreting coral stable oxygen isotope records of ENSO, *Clim. Past*, *9*(4), 1543–1557, doi:10.5194/cp-9-1543-2013.

Scholz, D., and D. L. Hoffmann (2011), Stalage—An algorithm designed for construction of speleothem age models, *Quat. Geochronol.*, *6*(3), 369–382, doi:10.1016/j.quageo.2011.02.002.

Scholz, D., D. L. Hoffmann, J. Hellstrom, and C. Bronk Ramsey (2012), A comparison of different methods for speleothem age modelling, *Quat. Geochronol.*, *14*, 94–104, doi:10.1016/j.quageo.2012.03.015.

Seimon, A. (2003), Improving climatic signal representation in tropical ice cores: A case study from the Quelccaya Ice Cap, Peru, *Geophys. Res. Lett.*, *30*(14), 1772, doi:10.1029/2003GL017191.

Shanahan, T. M., J. T. Overpeck, W. Sharp, C. A. Scholz, and J. A. Arko (2007), Simulating the response of a closed-basin lake to recent climate changes in tropical West Africa (Lake Bosumtwi, Ghana), *Hydrol. Processes*, *21*(13), 1678–1691, doi:10.1002/hyp.6359.

Smerdon, J. E., A. Kaplan, and D. E. Amrhein (2010), Erroneous model field representations in multiple pseudoproxy studies: Corrections and implications*, *J. Clim.*, *23*(20), 5548–5554, doi:10.1175/2010JCLI3742.1.

Smerdon, J. E., A. Kaplan, E. Zorita, J. F. González-Rouco, and M. N. Evans (2011), Spatial performance of four climate field reconstruction methods targeting the common era, *Geophys. Res. Lett.*, *38*, L11705, doi:10.1029/2011GL047372.

Spötl, C., I. J. Fairchild, and A. F. Tooth (2005), Cave air control on dripwater geochemistry, Obir Caves (Austria): Implications for speleothem deposition in dynamically ventilated caves, *Geochim. Cosmochim. Acta*, *69*(10), 2451–2468, doi:10.1016/j.gca.2004.12.009.

Spötl, C., A. Mangini, and D. A. Richards (2006), Chronology and paleoenvironment of Marine Isotope Stage 3 from two high-elevation speleothems, Austrian Alps, *Quat. Sci. Rev.*, *25*(9), 1127–1136, doi:10.1016/j.quascirev.2005.10.006.

Steig, E. J., et al. (2005), High-resolution ice cores from US ITASE (West Antarctica): Development and validation of chronologies and determination of precision and accuracy, *Ann. Glaciol.*, *41*(1), 77–84, doi:10.3189/172756405781813311.

Steig, E. J., et al. (2013), Recent climate and ice-sheet changes in West Antarctica compared with the past 2,000 years, *Nat. Geosci.*, *6*(5), 372–375, doi:10.1038/ngeo1778.

Steiger, N. J., G. J. Hakim, E. J. Steig, D. S. Battisti, and G. H. Roe (2014), Assimilation of Time-Averaged Pseudoproxies for Climate Reconstruction, *J. Clim.*, *27*(1), 426–441, doi:10.1175/JCLI-D-12-00693.1.

Steinman, B. A., M. B. Abbott, D. B. Nelson, N. D. Stansell, B. P. Finney, D. J. Bain, and M. F. Rosenmeier (2013), Isotopic and hydrologic responses of small, closed lakes to climate variability: Comparison of measured and modeled lake level and sediment core oxygen isotope records, *Geochim. Cosmochim. Acta*, *105*, 455–471.

Stoll, H. M., W. Müller, and M. Prieto (2012), I-STAL, a model for interpretation of Mg/Ca, Sr/Ca and Ba/Ca variations in speleothems and its forward and inverse application on seasonal to millennial scales, *Geochem. Geophys. Geosyst.*, *13*, Q09004, doi:10.1029/2012GC004183.

Sturm, C., Q. Zhang, and D. Noone (2010), An introduction to stable water isotopes in climate models: Benefits of forward proxy modelling for paleoclimatology, *Clim. Past*, *6*(1), 115–129, doi:10.5194/cp-6-115-2010.

Terwilliger, V. J. (2003), Influence of phenotypic plasticity in photosynthetic functions on the spatial distributions of tropical trees, *Phys. Geogr.*, *24*(5), 433–446, doi:10.2747/0272–3646.24.5.433.

Thompson, D. M., T. R. Ault, M. N. Evans, J. E. Cole, and J. Emile-Geay (2011), Comparison of observed and simulated tropical climate trends using a forward model of coral $\delta^{18}O$, *Geophys. Res. Lett.*, *38*, L14706, doi:10.1029/2011GL048224.

Thompson, D. M., T. Ault, M. Evans, J. Cole, J. Emile-Geay, and A. LeGrande (2013a), Coral-model comparison highlighting the role of salinity in long-term trends, *PAGES News*, *21*(2), 60–61.

Thompson, L., E. Mosley-Thompson, M. Davis, V. Zagorodnov, I. Howat, V. Mikhalenko, and P.-N. Lin (2013b), Annually resolved ice core records of tropical climate variability over the past$\sim$ 1800 years, *Science*, *340*(6135), 945–950, doi:10.1126/science.1234210.

Thompson, L. G., E. Mosley-Thompson, J. F. Bolzan, and B. R. Koci (1985), A 1500-Year Record of Tropical Precipitation in Ice Cores from the Quelccaya Ice Cap, Peru, *Science*, *229*, 971–973, doi:10.1126/science.229.4717.971.

Thompson, L. G., E. Mosley-Thompson, H. Brecher, M. Davis, B. Le'on, D. Les, P.-N. Lin, T. Mashiotta, and K. Mountain (2006), Abrupt tropical climate change: Past and present, *Proc. Natl. Acad. Sci. U. S. A.*, *103*(28), 10,536–10,543, doi:10.1073/pnas.0603900103.

Tierney, J. E., S. C. Lewis, B. I. Cook, A. N. LeGrande, and G. A. Schmidt (2011), Model, proxy and isotopic perspectives on the East African Humid Period, *Earth Planet. Sci. Lett.*, *307*(1), 103–112, doi:10.1016/j.epsl.2011.04.038.

Tierney, J. E., N. J. Abram, K. J. Anchukaitis, M. N. Evans, C. Giry, K. H. Kilbourne, C. P. Saenger, H. C. Wu, and J. Zinke (2015), Tropical sea surface temperatures for the past four centuries reconstructed from coral archives, *Paleoceanography*, *30*, doi:10.1002/2014PA002717, in press.

Tindall, J. C., P. J. Valdes, and L. C. Sime (2009), Stable water isotopes in HadCM3: Isotopic signature of El Niño-Southern Oscillation and the tropical amount effect, *J. Geophys. Res.*, *114*, D04111, doi:10.1029/2008JD010825.

Tingley, M. P., P. F. Craigmile, M. Haran, B. Li, E. Mannshardt, and B. Rajaratnam (2012), Piecing together the past: Statistical insights into paleoclimatic reconstructions, *Quat. Sci. Rev.*, *35*, 1–22, doi:10.1016/j.quascirev.2012.01.012.

Tolwinski-Ward, S. E., K. J. Anchukaitis, and M. N. Evans (2013), Bayesian parameter estimation and interpretation for an intermediate model of tree-ring width, *Clim. Past*, *9*(4), 1481–1493, doi:10.5194/cp-9-1481-2013.

Truebe, S. a., T. R. Ault, and J. E. Cole (2010), A forward model of cave dripwater $\delta^{18}O$ and application to speleothem records, *IOP Conf. Ser. Earth Environ. Sci.*, *9*, 012022, doi:10.1088/1755-1315/9/1/012022.

Vogel, J. C., J. C. Lerman, and W. G. Mook (1975), Natural isotopes in surface and groundwater from Argentina, *Hydrol. Sci. Bull.*, *2*, 203–221.

Vuille, M. (2003), Modeling $\delta^{18}O$ in precipitation over the tropical Americas: 2. Simulation of the stable isotope signal in Andean ice cores, *J. Geophys. Res.*, *108*(D6), 4174, doi:10.1029/2001JD002039.

Wackerbarth, A., D. Scholz, J. Fohlmeister, and A. Mangini (2010), Modelling the value of cave drip water and speleothem calcite, *Earth Planet. Sci. Lett.*, *299*(3–4), 387–397, doi:10.1016/j.epsl.2010.09.019.

Wackerbarth, A., P. Langebroek, M. Werner, G. Lohmann, S. Riechelmann, A. Borsato, and A. Mangini (2012), Simulated oxygen isotopes in cave drip water and speleothem calcite in european caves, *Clim. Past*, *8*(6), 1781–1799.

Wang, J., J. Emile-Geay, D. Guillot, J. E. Smerdon, and B. Rajaratnam (2014), Evaluating climate field reconstruction techniques using improved emulations of real-world conditions, *Clim. Past*, *10*(1), 1–19, doi:10.5194/cp-10-1-2014.

Weber, J. N., and P. M. Woodhead (1972), Temperature dependence of oxygen-18 concentration in reef coral carbonates, *J. Geophys. Res.*, *77*, 463–473.

Wellington, G. M., R. B. Dunbar, and G. Merlen (1996), Calibration of stable oxygen isotope signatures in Galápagos corals, *Paleoceanography*, *11*, 467–480.

Werner, M., P. M. Langebroek, T. Carlsen, M. Herold, and G. Lohmann (2011), Stable water isotopes in the ECHAM5 general circulation model: Toward high-resolution isotope modeling on a global scale, *J. Geophys. Res.*, *116*, D15109, doi:10.1029/2011JD015681.

Whillans, I., and P. Grootes (1985), Isotopic diffusion in cold snow and firn, *J. Geophys. Res.*, *90*, 3910–3918.

Williams, P. W. (2008), The role of the epikarst in karst and cave hydrogeology: A review, *Int. J. Speleol.*, *37*(1), 1.

Wilson, R., E. Cook, R. D'Arrigo, N. Riedwyl, M. N. Evans, A. Tudhope, and R. Allan (2010), Reconstructing ENSO: The influence of method, proxy data, climate forcing and teleconnections, *J. Quat. Sci.*, *25*(1), 62–78, doi:10.1002/jqs.1297.

Yurtsever, Y. (1975), *Worldwide Survey of Stable Isotopes in Precipitation*, *Rep. Isot. Hydrol. Sect.*, pp. 1–40, Int. At. Energy Agency, Vienna.